

# 1 Modeling tabular icebergs coupled to an ocean model

2 **A. A. Stern<sup>1</sup>, A. Adcroft<sup>1</sup>, O. Sergienko<sup>1</sup>, G. Marques<sup>1</sup>, R. Hallberg<sup>1</sup>**

3 <sup>1</sup>Geophysical Fluid Dynamics Laboratory, Princeton University  
4 <sup>1</sup>201 Forrestal Rd, Princeton, NJ 08540, USA

## 5 **Key Points:**

- 6
- 7
- 8
- 9
- 10
- A novel modeling framework is developed to explicitly model large tabular icebergs submerged in the ocean.
  - Tabular icebergs are constructed out of Lagrangian elements that drift in the ocean, and are held together by numerical bonds.
  - Breaking the numerical bonds allows us to model iceberg breakup and calving

11 **Abstract**

12 The calving of large tabular icebergs from the Antarctic ice shelves accounts for approxi-  
 13 mately half of Antarctic ice-shelf decay. After calving, these tabular icebergs drift across  
 14 large distances, altering regional ocean circulation, bottom-water formation, sea-ice pro-  
 15 duction and biological primary productivity in the icebergs' vicinity. However, despite  
 16 their importance, the current generation of numerical models is unable to represent large  
 17 tabular icebergs in a physically realistic way. In this study we develop a novel framework  
 18 to model large tabular icebergs submerged in the ocean. In this framework, tabular ice-  
 19 bergs are constructed out of Lagrangian elements that drift in the ocean, and are held to-  
 20 gether by numerical bonds. By breaking these bonds, a tabular iceberg can be made to  
 21 split into smaller pieces, or to break away from an ice shelf. We describe the Lagrangian  
 22 bonded iceberg model and discuss a number of the technical elements involved in its de-  
 23 velopment. We demonstrate the capabilities of the model by modeling a tabular iceberg  
 24 drifting away an idealized ice shelf.

25 **1 Introduction**

26 The Antarctic ice shelves are characterized by large infrequent calving events where  
 27 massive pieces of the ice shelves break off, to create large tabular icebergs. Observational  
 28 estimates suggest that over the past 30 years approximately half of Antarctic ice-shelf de-  
 29 cay is due to iceberg calving, while the other half occurs through ice-shelf melting [De-  
 30 poorter et al , 2013; Rignot et al , 2013]. Iceberg sizes appear to fit a power law distri-  
 31 bution, with the majority of icebergs being small ( $L < 1$  km), while the far less numerous  
 32 large tabular icebergs ( $L > 5$  km) account for more than 90% of Southern Hemisphere  
 33 iceberg mass [Tournadre et al , 2016].

34 After calving, icebergs slowly drift away from their source glaciers, often becom-  
 35 ing stuck in sea ice, or grounding along the Antarctic coast [Lichéy and Hellmer , 2001;  
 36 Dowdeswell and Bamber , 2007]. Large tabular icebergs extend deep into the water col-  
 37 umn, and have the potential to disrupt ocean circulation patterns for months or even years  
 38 after calving [Robinson et al , 2012; Stern et al , 2015]. The freshwater flux from iceberg  
 39 melt impacts ocean hydrography around the iceberg, influencing sea-ice production and  
 40 bottom-water formation [Arrigo et al , 2002; Robinson et al , 2012; Nicholls et al , 2009;  
 41 Fogwill et al , 2016]. The long distances traveled by large icebergs before melting means  
 42 that their meltwater impact is often felt hundreds of kilometers away from their calving  
 43 origins [Stern et al , 2016]. Meltwater injection (and the accompanying upwelling) from  
 44 icebergs can also influence biological productivity by providing nutrients to the surface  
 45 ocean or changing sea ice conditions [Arrigo et al , 2002; Vernet et al , 2012; Biddle et  
 46 al , 2015]. The increased productivity associated with free-floating tabular icebergs has  
 47 been linked with local increases in ocean carbon uptake, potentially large enough to be a  
 48 significant fraction of the Southern Ocean carbon sequestration [Smith et al , 2007].

49 In recent years, there has been an increased interest in iceberg drift and decay. This  
 50 surge of interest has been driven by (i) the need to understand polar freshwater cycles  
 51 in order to create realistic climate forecasts and sea level projections [Silva et al , 2006;  
 52 Shepherd and Wingham , 2007; Rignot et al , 2013]; and (ii) the increased use of high-  
 53 latitudes iceberg-filled waters for shipping lanes and offshore hydrocarbon exploration  
 54 in the Arctic [Pizzolato et al , 2012; Unger , 2014; Henderson and Loe , 2016]. The in-  
 55 creased interest in icebergs has led to the development of numerical models of iceberg  
 56 drift and decay [Mountain , 1980; Bigg et al , 1997; Gladstone et al , 2001; Kubat et al  
 57 , 2005], some of which have been included in global General Circulation Models [Mar-  
 58 tin and Adcroft , 2010; Marsh et al , 2015]. These iceberg drift models treat icebergs as  
 59 Lagrangian point particles, which are advected by the flow, and melt according to cer-  
 60 tain parameterizations for icebergs melt. Since icebergs are treated as point particles, ice-  
 61 berg drift models are mostly suitable for modeling icebergs smaller than an ocean grid

62 cell. Consequently, these models have mostly been used to represent icebergs smaller than  
 63 3.5 km on a global scale [Jongma et al , 2009; Martin and Adcroft , 2010; Marsh et al ,  
 64 2015].

65 Point-particle iceberg drift models are less suitable for modeling larger tabular ice-  
 66 bergs, where the size and structure of the iceberg may be an important feature in deter-  
 67 mining their drift and decay [Stern et al , 2016]. They also are not suitable for studying  
 68 the local effects that icebergs have on the surrounding ocean, or the small scale processes  
 69 that influence iceberg melt and decay [Wagner et al , 2014; Stern et al , 2015]. For this  
 70 reason, tabular icebergs ( $L > 5$  km) are currently not represented in the iceberg drift mod-  
 71 els used in climate models, even though observations suggest that tabular icebergs account  
 72 for the vast majority of the total Southern Hemisphere iceberg mass [Tournadre et al ,  
 73 2016].

74 The goal of this study is to develop a new iceberg model where tabular icebergs are  
 75 explicitly resolved. In this model, icebergs are no longer treated as point particles that in-  
 76 teract with the ocean at a single location, but rather icebergs are given structure, so that  
 77 they interact with the ocean across multiple ocean grid cells and depress the ocean surface  
 78 over a wide area. To do this, we create tabular icebergs out of many Lagrangian elements  
 79 with finite extent which are ‘bonded’ together by numerical bonds. The numerical bonds  
 80 hold the ice elements together and allow a collection of elements to move as a unit (see  
 81 schematic in Figure 1). By manually breaking these bonds, we can simulate iceberg calv-  
 82 ing, allowing us to study the ocean response to a large tabular iceberg detaching from an  
 83 ice shelf (e.g.: Figure 2 and 3) or the fracturing of a large iceberg into smaller pieces.

84 The Lagrangian model developed in this study is referred to at the Lagrangian Bonded  
 85 Iceberg Model (LBIM). Section 2 gives a description of many of the key aspects of the  
 86 LBIM. Since this model is a new approach to modeling icebergs, we present many of the  
 87 technical elements involved in constructing the model. In section 3 and 4, we demonstrate  
 88 the capabilities of the model by simulating a tabular iceberg detaching from an idealized  
 89 ice shelf.

## 90 2 Model description

91 The LBIM is a Lagrangian particle-based model (or discrete element model) in that  
 92 the objects of the model are Lagrangian elements. Each element represents a mass of ice  
 93 that is floating in the ocean, and has a position, velocity, mass, and a set of dimensions,  
 94 which can evolve in time. The motion of each element is determined by a momentum  
 95 equation which is solved in the (Lagrangian) reference frame of the element. The ele-  
 96 ments are forced by oceanic and atmospheric forces, which are provided by the user, or  
 97 are determined by coupling the LBIM to an ocean/atmosphere model. The elements also  
 98 interact with one another and can be bonded together to form larger structures. The an-  
 99 gular momentum of the elements is not modeled explicitly; instead rotational motion of  
 100 larger structures emerge as a consequence of bond orientation and collective motion. In  
 101 different contexts, the LBIM elements can be thought to represent individual icebergs, sea  
 102 ice flows, or, when the elements are bonded together, they can represent larger structures  
 103 such as tabular icebergs or ice shelves.

104 The LBIM is developed on the code base of an existing iceberg drift model [Martin  
 105 and Adcroft , 2010; Stern et al , 2016]. When run with the correct set of runtime flags,  
 106 the model runs as a traditional iceberg drift model.

### 107 2.1 Equations of motion

108 The elements drift in the ocean, forced by atmosphere, ocean and sea-ice drag forces,  
 109 as well as the Coriolis force and a force due to the sea surface slope. When these ice el-

ements move alone (without interactions with other elements), they can be thought of as representing individual (or clusters of) small icebergs, and follow the same equations described in the iceberg drift model of Martin and Adcroft [2010] (based on the equations outlined in Bigg et al [1997] and Gladstone et al [2001]).

In addition to the environmental forces, the elements in the LBIM experience interactive forces due to the presence of other elements. Two types of interactive forces are included between elements. The first force is a repulsive force which is applied to elements to prevent them from moving too close to one another. This repulsive force prevents icebergs from piling up on top of one another. The second interactive force is a force due to numerical ‘bonds’, and is only applied if two elements are labelled as ‘bonded’. When two elements are bonded, each element feels an attractive force that prevents the elements from moving too far apart from one another. The interactive forces between two bonded elements are defined such that in the absence of other forces the elements come to rest adjacent to one another, with no overlap of the iceberg areas.

The momentum equation for each element is given by

$$M \frac{D\vec{u}}{Dt} = \vec{F}_A + \vec{F}_W + \vec{F}_R + \vec{F}_C + \vec{F}_{SS} + \vec{F}_{SI} + \vec{F}_{IA}, \quad (1)$$

where  $\frac{D}{Dt}$  is the total (Lagrangian) derivative,  $M$  is the mass of the element,  $\vec{u}$  is the velocity of the element, and the terms on the right hand side give the forces on the element due to air drag ( $\vec{F}_A$ ), water drag ( $\vec{F}_W$ ), sea ice drag ( $\vec{F}_{SI}$ ), Coriolis force ( $\vec{F}_C$ ), wave radiation force ( $\vec{F}_R$ ), sea surface slope ( $\vec{F}_{SS}$ ), and interactions with other elements ( $\vec{F}_{IA}$ ). The environmental forces are the same as those presented in Martin and Adcroft [2010], and are provided for completeness in Appendix A. The details of the interactive forces are provided in below.

## 2.2 Interactive Forces

The interactive force on an element is calculated by adding together the interactions with all other elements, such that the interactive force on element  $i$ ,  $(\vec{F}_{IA})_i$  is given by:

$$(\vec{F}_{IA})_i = \sum_{j \neq i} (\vec{F}_{IA})_{ij}, \quad (2)$$

where  $(\vec{F}_{IA})_{ij}$  is the force on element  $i$  by element  $j$ . Both bonded and repulsive interactions are modeled using elastic stresses with frictional damping. The elastic component of the force is a function of the distance between the two elements, while the frictional damping force depends on the relative velocity of the two elements.

To describe the forces between two elements, we begin by introducing some notation. Let  $\vec{x}_i$ ,  $\vec{x}_j$  be the positions of elements  $i$  and  $j$ . The distance between elements  $i$  and  $j$  is

$$d_{ij} = |\vec{x}_i - \vec{x}_j|. \quad (3)$$

When calculating the interactive forces between elements, the elements are assumed to be circular. We define the interaction diameter of an element by

$$D_i = 2 \sqrt{\frac{A_i}{\pi}}, \quad (4)$$

where  $A_i$  is the planar surface area of element  $i$ . Using this, we define the critical interactive length scale,

$$L_{ij} = \frac{D_i + D_j}{2}, \quad (5)$$

which governs interactions between elements  $i$  and  $j$ . Repulsive forces are only applied when  $d_{i,j} < L_{i,j}$ , while for  $d_{i,j} > L_{i,j}$  attractive bonded forces are applied when a bond exists between element  $i$  and  $j$ . Bond and repulsive forces are designed such that in the

absence of other forces, bonded particles will settle in an equilibrium position where elements are separated by the critical interaction length scale  $L_{i,j}$ .

To aid in notation, we define a bond matrix  $B_{ij}$  such that  $B_{ij} = 1$  if elements i and j are bonded together and  $B_{ij} = 0$  otherwise. Using this notation, the interactive force  $(\vec{F}_{IA})_{ij}$  on an element i by an element j is given by

$$(\vec{F}_{IA})_{ij} = \begin{cases} (\vec{F}_e)_{ij} + (\vec{F}_d)_{ij} & \text{if } d_{ij} \leq L_{ij} \\ (\vec{F}_e)_{ij} + (\vec{F}_d)_{ij} & \text{if } d_{ij} > L_{ij} \text{ and } B_{ij} = 1 \\ 0 & \text{if } d_{ij} > L_{ij} \text{ and } B_{ij} = 0 \end{cases} \quad (6)$$

$(\vec{F}_e)_{ij}$  and  $(\vec{F}_d)_{ij}$  are the elastic and frictional damping components of the interactive force between elements i and j. The elastic force  $(\vec{F}_e)_{ij}$  between elements is given by

$$(\vec{F}_e)_{ij} = -\kappa_e (d_{i,j} - L_{i,j}) T_{i,j} \vec{r}_{ij}, \quad (7)$$

where  $\vec{r}_{ij} = \frac{(\vec{x}_i - \vec{x}_j)}{|\vec{x}_i - \vec{x}_j|}$  is the directional unit vector between the position of element i and j,  $\kappa_e$  is the spring constant, and  $T_{i,j}$  is the minimum of the thickness of elements i, j. The interactive forces obey Newton's 3rd Law (i.e.:  $(\vec{F}_{IA})_{ij} = -(\vec{F}_{IA})_{ji}$ ). The minimum thickness,  $T_{i,j}$ , is preferred to the average thickness, since this means that for two bonded elements a fixed distance apart, the acceleration due to elastic forces is bounded, even when the thickness of one of the elements approaches zero.

The frictional damping force has components that damp both the relative radial velocity and relative transverse velocities of the two elements. If  $\vec{r}_{ij}^\perp$  is the direction vector perpendicular to  $\vec{r}_{ij}$ , and  $P_{\vec{r}_{ij}}$  and  $P_{\vec{r}_{ij}^\perp}$  are the projection matrices that project onto  $\vec{r}_{ij}$  and  $\vec{r}_{ij}^\perp$  respectively, then the frictional damping force is given by

$$(\vec{F}_d)_{ij} = \left( -c_r P_{\vec{r}_{ij}} - c_t P_{\vec{r}_{ij}^\perp} \right) \cdot (\vec{u}_i - \vec{u}_j) \quad (8)$$

Here  $c_r$  and  $c_t$  are the radial and transverse drag coefficients. For the simulation below, we set  $c_r = 2\sqrt{\kappa_e}$  and  $c_t = \frac{1}{4}c_r$  so that the radial elastic force is critically damped, and the transverse damping is sub critical. The damping forces are implemented using an implicit time stepping scheme, to avoid stability issues for very small elements (details found in Appendix B).

The effectiveness of the repulsive forces can be seen in Figure 4, which shows an uncoupled (ice only) simulation where ice elements drift westward into a bay, and eventually come to rest with minimal overlap between elements. The effectiveness of the numerical bonds is demonstrated in Figure 5, where tabular icebergs (constructed from many ice elements bonded together) and individual icebergs (unbonded elements) drift together towards a convex coast line. When the tabular icebergs arrive at the coast, they bump into the coastline and begin to rotate, influencing the paths of the other icebergs. In this example we see that modeling large structures using small elements bonded together, allows us to achieve large-scale structure and rotational motion, without having to include an equation for the angular momentum of the elements (as discussed in Jakobsen [2001]). Animations of these uncoupled simulations can be found in the supplementary materials.

### 2.3 Initializing element geometry and packing

For purposes of packing, we assume that elements have surface areas which are shaped as equally-sized regular hexagons (note that the elements are assumed to be circular for purposes of interactions, but are assumed to be hexagonal for packing purposes). When packing these elements together, the hexagonal elements are initially arranged in a staggered lattice, with each element bonded to the adjacent elements (see Figure 1). In this arrangement, each element (away from the edges) is bonded to six other elements.

189 The bonds between elements form a pattern of equilateral triangles, which give the larger  
 190 structure rigidity. The circular shape of elements (used for interactions) is inscribed within  
 191 the hexagonal shape used for packing (Figure 1). The centers of adjacent elements are ini-  
 192 tially separated by a distance  $d_{i,j} = L_{i,j} = 2A_p$ , where  $A_p$  is the length the apothems of  
 193 the hexagons.

194 Some experiments were also performed using rectangular elements, arranged in a a  
 195 regular (non-staggered) lattice. In this case, each element forms four bonds with adjacent  
 196 elements. However, the resultant structures were found to be much less rigid and tended  
 197 to collapse when sufficient forces was applied. For this reason, hexagonal elements are  
 198 used here.

## 199 2.4 Ocean-ice and ice-ocean coupling

200 The LBIM is coupled to the ocean model via a two-way synchronous coupling,  
 201 meaning that ocean-model fields are passed to the LBIM, and the LBIM fields are passed  
 202 back to the ocean model at every time step. Passing fields between the two models in-  
 203 volves interpolating the fields from the ocean model's Eulerian grid onto the LBIM's 'La-  
 204 grangian grid' (i.e.: onto the ice elements, Figure 1), and aggregating fields from the La-  
 205 grangian elements onto the ocean-model's Eulerian grid.

206 The coupling from the ocean model to the LBIM is straight forward: at every time  
 207 step, the ocean mixed layer temperature, salinity, velocity and sea-ice concentration are  
 208 passed from the ocean model to the LBIM, to be used in the momentum and thermo-  
 209 dynamic equations of the ice elements. Since tabular icebergs are explicitly resolved in  
 210 the ocean, it is sufficient for each element to interact with ocean mixed layer only (i.e.:  
 211 there is no need to manually embed icebergs into the ocean by integrating ocean fields  
 212 over the icebergs' thickness, as suggested in Merino et al [2016]). Within the LBIM, the  
 213 ocean model fields are interpolated onto the Lagrangian grid using a bilinear interpolation  
 214 scheme.

215 The coupling from the LBIM to ocean model is more complex. The LBIM influ-  
 216 ences the ocean by: (i) applying a pressure to the ocean surface, (ii) affecting the upper  
 217 ocean by applying a no-slip boundary condition and frictional velocity beneath the ice,  
 218 and (iii) imposing heat, salt and mass fluxes on the ocean, associated with ice melting.  
 219 Six fields are passed from the LBIM to the ocean model: ice mass, ice area, frictional ve-  
 220 locity, heat flux, salt flux, and mass flux. Fields from the LBIM are aggregated from the  
 221 Lagrangian elements to the Eulerian ocean grid before they are passed to the ocean model.

222 The aggregation of the LBIM fields onto the ocean grid is done in a way that is  
 223 consistent with the shape of the elements in the LBIM (see Section 2.3). Fields are 'spread'  
 224 to the ocean model grid by exactly calculating what fraction of an element's surface area  
 225 lies in a particular grid box, and dividing the field in proportion to this fraction. For ex-  
 226 ample, consider a hexagonal element in the LBIM, which is positioned such that it inter-  
 227 sects four ocean grid cells (inset panel in Figure 1). In this situation, the mass of the ele-  
 228 ment is divided between these four ocean cells in proportion to the overlap area between  
 229 the hexagonal element and the grid cell (this fraction is shown by the colors in the inset  
 230 panel in Figure 1). An advantage of this approach is that there are no jumps in pressure as  
 231 an element moves from one grid cell to another, which could trigger tsunamis within the  
 232 ocean model, making the ocean model unrealistic..

233 The numerical calculation of the intersection between hexagons and the ocean grid  
 234 is simplified by dividing the hexagon into 6 equilateral triangles. This method allows for  
 235 the intersection to be found even when the hexagon is not aligned with the grid.

236 The aggregation scheme is coded with the restriction that an element's area can only  
 237 intersect a maximum of four ocean grid cells at a time. A consequence of this is that this

sets a limit on the maximum size of elements that can be represented using this model, i.e.: the longest horizontal dimension of an ice element must be smaller than the ocean grid spacing. Larger ice structures are constructed by bonding together smaller elements.

## 2.5 Thermodynamics

The ice elements decay according to a number of melt parameterizations. As the ice elements melt, their mass decreases, and the appropriate salt, mass and heat fluxes are passed to the ocean. In this section we described the melt parametrization for bonded, unbonded and partially bonded elements.

As mentioned above, ice elements which do not interact with other elements are modeled identically to the point particle icebergs described in Martin and Adcroft [2010]. These elements melt according to three semi-empirical parametrization for melt commonly used in previous iceberg studies [Gladstone et al , 2001; Martin and Adcroft , 2010]. Three types of iceberg melting are used: basal melt,  $M_b$ , melt due to wave erosion,  $M_e$  and melt due to buoyant convection,  $M_v$ .  $M_e$  and  $M_v$  are applied to the sides of the ice element, while  $M_b$  is applied at the ice element base. The details of  $M_b$ ,  $M_v$  and  $M_e$  are given in Appendix A.

When multiple elements are bonded together to form larger structures, it is no longer appropriate to use the parameterizations for melt developed for individual point-particle icebergs. An element which is completely surrounded by other elements, is meant to represent a piece of ice in the middle of a large structure, and hence will not experience a melt at its sides due to wave erosion or buoyant convection. Also, the iceberg basal melt rate,  $M_b$  described above is based on boundary layer theory of flow past a finite plate, and is only appropriate for basal surfaces where the distance from the leading edge is sufficiently small [Eckert , 1950; Weeks and Campbell , 1973]. For an element in the interior of large structures, the distance from the edge of the structure is large, and so using  $M_b$  for the basal melt is not appropriate. Instead, the basal melt,  $M_s$  is determined using the three equation model for basal melt, which is a typical melting parametrization beneath used beneath ice shelves [Holland and Jenkins , 1999].

When using both individual elements and bonded elements in the same simulation, we determine which melt rate parameterizations to use based on the amount of bonds that each element has. An element which is in the center of a large structure will form the maximum number of bonds, while unbonded elements form zero bonds. If maximum number of bonds that an element can form (given the shape of the element) is  $N_{max}$ , and the number bonds that an element has is  $N_b$ , then the side melt and bottom melt for that element are given by

$$M_{side} = \frac{(N_{max} - N_b)}{N_{max}}(M_v + M_e) \quad (9)$$

and

$$M_{bottom} = \frac{(N_{max} - N_b)}{N_{max}}M_b + \frac{N_b}{N_{max}}M_s \quad (10)$$

respectively. In this way, elements with no bonds, melt like point-particle icebergs, elements at the center of large structures melt like ice shelves, and elements at the sides of large structures have a combination of iceberg side and basal melt, and ice-shelf melt.

## 2.6 Algorithms and computational efficiency

Including interactions between elements leads to an increase in the computational complexity of the model. In this subsection we comment on some of the algorithmic procedures that have been used to increase the computational efficiency.

281            **2.6.1 Interactions and Bonds**

282            At every time step, we calculate the force on each element due to interactions with  
 283            every other element. In principle, this involves order  $N^2$  operations (for N elements).  
 284            However, since each element only has repulsive interactions with elements that are less  
 285            than one ocean grid cell away, and each element only has bonded interactions with a  
 286            small number of other elements, we are able to reduce the complexity of the system.

287            The complexity reduction is achieved by storing the element data in an efficient way  
 288            that prevents having to search through all element pairs to check if they are close to one  
 289            another or are bonded with one another. The data storage system works as follows: pointers  
 290            to the memory structures containing each element are stored in linked list data struc-  
 291            tures, which allow elements to be added and removed from the lists easily without re-  
 292            structuring the entire list. Instead of using one list for all the elements on a processor (as  
 293            was done in the original code [Martin and Adcroft , 2010]), we use a separate linked list  
 294            for each ocean grid cell. When an element moves between ocean grid cells, it is removed  
 295            from its original list and added to the list corresponding to its new ocean grid cell. Since  
 296            the area of elements has to be smaller than the area of an ocean grid cell, the critical in-  
 297            teraction length scale (equation 5) is less than the length of a grid cell. This means that  
 298            elements only experience repulsive forces with other elements in the same ocean grid cell,  
 299            or in one of the 8 adjacent cells. At each time step and for each element  $i$ , the code tra-  
 300            verses these linked lists of the 9 surrounding grid cells, and applies a repulsive force if  
 301             $d_{i,j} < L_{ij}$  (whether the elements are bonded or not). Limiting the possible repulsive in-  
 302            teractions to elements in these 9 linked lists substantially reduces the computational time  
 303            needed to calculate the total interactive forces.

304            The attractive part of the bonded interactions are handled separately. Each bond is  
 305            assigned a piece of memory. Each ice element contains a linked list of each of its bonds  
 306            (typically up to six bonds per element). At every time step, the code traverses the lists  
 307            of bonded elements, and adds an attractive bonded force corresponding to these bonds if  
 308             $d_{i,j} > L_{ij}$  (the repulsive bonded force to be applied when  $d_{i,j} < L_{ij}$  is already accounted  
 309            for by the procedure outlined in the previous paragraph). Having a list of bonds stored  
 310            with each element reduces the computational complexity of bonded interactions from  
 311            order  $N^2$  to order N. Handling bonded attractive forces separately to the repulsive and  
 312            non-bonded forces means that we do not need to check whether two elements are bonded,  
 313            which further increases the computational efficiency.

314            **2.6.2 Parallelization and halos**

315            The LBIM runs on multiple processors in parallel (using the same grid decomposi-  
 316            tion as the ocean model). When elements move from an ocean cell on one processor to  
 317            an ocean cell on a second processor, the memory has to be passed from one processor the  
 318            next, added and removed to the appropriate lists and the memory has to be allocated and  
 319            deallocated correctly. Element interactions across the edge of processors are handled us-  
 320            ing computational halos. A computational halo is a copy of the edge of a one processor  
 321            which is appended to the edge of a second processor, so that the first processor can ‘see’  
 322            the second processor during a time step. Before each time step, elements at the edges of  
 323            each processor are copied onto the halos of adjacent processors so that they can be used  
 324            in calculating the interactive forces. After each time step, these halos are removed, and  
 325            the process is repeated. These halo updates are one of the most computationally expensive  
 326            parts of the LBIM.

327            Keeping track of pairs of bonded elements that move across a processor edge re-  
 328            quires a lot of book keeping since bonds have to be severed and reconnected. Details of  
 329            how the bonds are broken and reconnected across processor boundaries are provided in  
 330            Appendix C.

331      **2.6.3 Time stepping**

332      The ice elements in the LBIM are advected using a semi-implicit velocity Verlet  
 333      time-stepping scheme. The velocity Verlet time stepping scheme is commonly used in dis-  
 334      crete element models in video games because it is computational efficient and has desir-  
 335      able stability properties [Jakobsen , 2001]. This time stepping scheme was preferred to the  
 336      Runge-Kutta 4, which was used in the iceberg model of Martin and Adcroft [2010] since  
 337      the Verlet time stepping only requires one calculation of the interactive forces once per  
 338      time step (while the Runge-Kutta scheme requires the interactive forces to be calculated  
 339      four times). Since the calculation of the interactive forces is one of the most computa-  
 340      tionally expensive part of the algorithm, the Verlet scheme leads to a significant increase  
 341      in the speed of the model. We note that the Verlet scheme used in the LBIM contains a  
 342      modification of the original (fully explicit) velocity Verlet time stepping scheme in that  
 343      damping terms are treated implicitly (which increases the numerical stability). The details  
 344      of this time stepping scheme are outlined in Appendix B.

345      **3 Experiment Setup**

346      The introduction of Lagrangian elements, numerical bonds and interpolation schemes  
 347      between the Eulerian and Lagrangian grids (discussed in Section 2) means that we now  
 348      have the tools to model large tabular icebergs submerged in the ocean. We demonstrate  
 349      this capability by simulating a tabular iceberg drifting away from an idealized ice shelf.

350      **3.1 Model configuration**

351      We initialized our simulation using the experimental setup created for the Marine  
 352      Ice Ocean Modeling Inter-comparison Project (MISOMIP) [Asay-Davis et al , 2016]. The  
 353      configuration consists of an idealized ice shelf in a rectangular domain. The domain is  
 354       $L_x = 80$  km wide and  $L_y = 480$  km long, and contains an ice shelf which is grounded on  
 355      the south side of the domain and has an ice front at  $y=650$  km. The ice thickness and  
 356      bottom topography of this setup are shown in Figure 6a and 6b respectively, with the  
 357      grounding line position drawn in for reference. The configuration is the same as that of  
 358      the Ocean0 setup in the MISOMIP, with a few minor changes to the ice-shelf geometry  
 359      (see Supplementary Material for details).

360      **3.2 Initializing Lagrangian elements:**

361      The idealized ice shelf is constructed out of Lagrangian ice elements. Ice elements  
 362      are hexagonal and are arranged in a regular staggered lattice (as discussed in Section 2.3).  
 363      The sides of the gridded hexagons are initialized with length  $S = 0.98$  km. Gaps along  
 364      the boundaries are filled in using smaller elements so that the total ice-shelf area is pre-  
 365      served. The initial mass of the ice elements is determined by a preprocessing inversion  
 366      step, which is the inverse of the ‘mass-spreading’ aggregation procedure discussed in Sec-  
 367      tion 2.3. The ice draft calculated without mass-spreading aggregation (treating elements  
 368      as point masses) contains large grid artifacts (Figures 6c). These grid artifacts are much  
 369      reduced after the mass-spreading aggregation is applied (Figure 6b).

370      **3.3 Ocean model setup**

371      The LBIM is coupled to the MOM6 ocean model [Hallberg et al , 2013]. The ocean  
 372      model is run using a vertical coordinate system which is a hybrid between a sigma-level  
 373      and a z-level coordinate. In particular, model layers bend underneath the ice shelf as they  
 374      would in a sigma-coordinate model, but collapse to zero thickness when they intersect  
 375      with bottom topography, as they would in a z-level model. The coordinate system was  
 376      achieved using ALE regridding-remapping scheme [White et al , 2009]. The model uses a

377 horizontal resolution of 2 km, and 72 vertical layers. All simulations were repeated using  
 378 the ocean model configured in isopycnal mode (results were similar and are not presented  
 379 here).

380 Ocean parameters are as specified in the MISOMIP configuration [Asay-Davis et  
 381 al , 2016], and are shown in Table 1. The simulation is initially at rest, with horizontally  
 382 uniform initial ocean temperature and salinity profiles which vary linearly between spec-  
 383 ified surface and bottom values:  $T_{top} = -1.9^\circ \text{C}$ ,  $T_{bottom} = 1.0^\circ \text{C}$ ,  $S_{top} = 33.8 \text{ psu}$ ,  
 384  $S_{bottom} = 34.7 \text{ psu}$ . The maximum ocean depth is  $H_{ocean} = 720 \text{ m}$ . A sponge layer is  
 385 used on the northern boundary, which relaxes back to the initial temperature and salinity  
 386 with a relaxation time scale of  $T_{sponge} = 0.1 \text{ days}$ . Melting is set to zero for ocean cells  
 387 where the ocean column thickness is less than 10m to avoid using more energy to melt ice  
 388 than is present in the water column.

### 389 **3.4 Spinup period:**

390 The model is spun up for 5 years with all ice elements being held stationary. Dur-  
 391 ing spinup, the injection of buoyant meltwater at the base of the ice shelf drives a clock-  
 392 wise circulation within the domain (not shown). The circulation compares well with an  
 393 identical static ice-shelf experiment run using an Eulerian ice shelf model [Goldberg et al  
 394 , 2012]. A detailed comparison of the Lagrangian and Eulerian ice shelf models is pre-  
 395 sented in a separate study, and is not shown here.

### 396 **3.5 Iceberg calving:**

397 After spinup, a large tabular iceberg is ‘broken off’ from the ice shelf, and allowed  
 398 to drift into the open ocean. This is achieved by allowing all ice elements initially within  
 399 a 14.4 km radius of the center of the ice front to move freely while the other ice ele-  
 400 ments continue to be held stationary. Ice elements less than 12 km from the center of  
 401 the ice front, are bonded together to form a semi-circular tabular iceberg. A ring of el-  
 402 ements whose distance,  $d$ , from the ice front center obeys  $12 \text{ km} \leq d \leq 14.4 \text{ km}$ , are  
 403 allowed to move freely, but have all their bonds removed. Elements in this half annulus  
 404 represent fragments of the ice shelf which calve into small pieces during a large calv-  
 405 ing event. Breaking the bonds of these surrounding elements allows the tabular iceberg  
 406 to move away from the ice-shelf cavity more easily.

### 407 **3.6 Wind stress and bond breaking:**

408 After the spinup period, a wind stress  $\vec{\tau} = < \tau_x, \tau_y > = < 0.05, 0.05 > \frac{N}{m^2}$  is applied to  
 409 drive the tabular iceberg away from the ice-shelf cavity. This is referred to as the control  
 410 simulation. Perturbation experiments were also performed using other wind stress values.  
 411 Further perturbation experiments were performed by manually breaking some numerical  
 412 bonds in order to break the tabular iceberg into smaller pieces.

## 413 **4 Model Results**

414 After spinup, the elements near the ice-shelf front are allowed to move freely, and  
 415 the icebergs begin to drift away from the ice shelf while fully submerged in the ocean  
 416 (see figures 2 and 7, and the animations in the supplementary materials). At this point  
 417 the LBIM and the ocean model are fully-coupled: changes to the iceberg position alter  
 418 the top-of-ocean pressure and dynamical boundary condition; and changes to the iceberg  
 419 melt rates alter the top-of-ocean temperature, salt and mass fluxes. These changing ocean  
 420 boundary conditions influence the ocean by triggering gravity waves, driving surface mix-  
 421 ing, affecting the ocean stratification, and creating ocean instabilities. The evolving ocean  
 422 velocities, temperatures and salinities feedback onto the ice elements by changing the

423 force balance on the ice elements (leading to changes in the elements' position), and al-  
 424 tering the melt rates. The various feedbacks within this coupled system offer many oppor-  
 425 tunities for the model to become unstable. The fact that the model is stable and that we  
 426 are able to simulate tabular icebergs moving in the ocean without the modeling crashing,  
 427 is a non-trivial technical milestone.

#### 428 4.1 Icebergs' motion

429 In the control simulation, the semi-circular tabular iceberg moves as a cohesive unit  
 430 due to the presence of the numerical bonds, while the smaller ice fragments quickly dis-  
 431 perse (Figure 2). The tabular iceberg drifts towards the northward east, driven by the wind  
 432 and steered by the Coriolis force. As the tabular iceberg drifts northwards, it rotates in a  
 433 counterclockwise direction, and makes contact with the eastern boundary of the domain,  
 434 before continuing northward. Most of the smaller ice fragments also move to the north-  
 435 east, but not as a cohesive unit. Some of these element also move rapidly to other parts of  
 436 the domain.

437 The direction (and speed) of the iceberg drift is largely determined by the wind  
 438 speed and direction. Perturbation experiments using different wind stresses show that for  
 439 sufficiently large winds, the tabular iceberg drifts to the north east when  $\tau_x > 0$ , and to the  
 440 north west when  $\tau_x < 0$  (not shown). For a purely zonal wind stress with  $|\tau_x| \leq 0.01 \frac{N}{m^2}$ ,  
 441 the iceberg does not move away from the ice shelf. When the wind is purely offshore  
 442 ( $\tau_x = 0.0 \frac{N}{m^2}$ ), a meridional wind stress  $\tau_y \geq 0.05 \frac{N}{m^2}$  is needed to move the tabular ice-  
 443 berg away from the ice shelf. While this result is partly an artifact of the artificial shape  
 444 of the calving iceberg, it is also consistent with Bassis and Jacobs [2013] who noted that  
 445 calving is a two step process consisting of (i) ice-shelf breaking and (ii) iceberg detach-  
 446 ment. The results here suggest that strong (cross-shore) winds may be required to drive  
 447 large tabular icebergs away from their source glaciers.

#### 448 4.2 Breaking bonds

449 The numerical bonds in the LBIM are needed in order to allow the tabular iceberg  
 450 to retain its shape. This is demonstrated by comparing the control simulation to an identi-  
 451 cal simulation where all numerical bonds have been removed (Figure 10). In the bond-free  
 452 simulation, the absence of the bonds means that there is no force holding the tabular ice-  
 453 berg together, and the ice elements quickly move apart from one another (Figure 10b).  
 454 This bond-free simulation does not adequately represent tabular iceberg, which can move  
 455 long distances through the ocean as a cohesive unit. This result motivates the inclusion of  
 456 numerical in the LBIM model, even though they are computationally expensive. Breaking  
 457 multiple bonds simultaneously could be used to simulate ice shelf disintegration events.

458 By breaking some (but not all) numerical bonds, we can simulate the fracturing of  
 459 tabular icebergs, and allow tabular icebergs to break into smaller pieces. Figure ??? shows  
 460 the results of an experiment which is indentical to the control experiment, except that all  
 461 numerical bonds that intersect the line  $x = \frac{L_x}{2}$  have been severed. This effectively cuts the  
 462 large tabular iceberg into two halves. As the icebergs drift northwards, the two halves of  
 463 the tabular iceberg each move as a cohesive unit, but they are able to move independently  
 464 of one other (Figure ???). The two large fragments initially move together, but begin to  
 465 separate after a few days. The breaking of a tabular iceberg has the additional effect of in-  
 466 creasing the total surface area of ice exposed to the ocean, thus increasing the total decay  
 467 rate of the ice.

#### 468 4.3 Ocean response

469 Since the tabular iceberg is submerged in the ocean, the iceberg calving and drift  
 470 affects the the surrounding ocean. In the control simulation, as the tabular iceberg drifts

471 northward a warming of the surface waters is observed around the tabular iceberg, with  
 472 the largest warming occurring at the ice-shelf front and along the tabular iceberg's rounded  
 473 edge (Figure 3). This surface warming is caused by upwelling of the warmer waters from  
 474 beneath the ice shelf and iceberg. As the icebergs drifts away from the ice shelf, these  
 475 warmer waters remain at the surface, mapping of the wake of the iceberg (Figure 3). The  
 476 motion of the tabular iceberg disturbs the ocean surface, which drives ocean velocities  
 477 through out the water column (Figure 8). The elevated shears around the tabular iceberg  
 478 lead to increased vertical mixing in the vicinity of the iceberg, which alters the stratifica-  
 479 tion of the water column (Figure 7), heating the upper ocean. The signature of upwelling  
 480 water in the wake of a drifting tabular iceberg bears some similarity to satellite observa-  
 481 tions of streaks of increased ocean color in the wake of tabular iceberg in the Southern  
 482 Ocean [Duprat et al , 2016], suggesting that the increased productivity around icebergs  
 483 may be driven by upwelling water delivering nutrients to the surface.

#### 484 4.4 Iceberg melt rates

485 The increased top-of-ocean velocities and temperatures cause elevated melt rates at  
 486 the base of the ice shelf and iceberg (Figure 9). The largest melt rates are observed at the  
 487 newly calved ice-shelf front and on the rounded side of the tabular iceberg (Figure 9a),  
 488 where the iceberg calving has created steep ice cliffs. These sharp ice fronts allow for  
 489 large ocean currents (Figure 9c), which drive the elevated melt rates. The elevated melt  
 490 rates act to smooth out the ice front over time, making the ice cliff less steep. While this  
 491 is likely a real phenomena that could be observed in nature, we should be wary of the  
 492 modeled velocities at the ice cliffs, since large changes in ice thicknesses are often associ-  
 493 ated with numerical pressure gradient errors which can drive spurious motion.

494 The large melt rates along the ice edges are also partly driven by the fact that differ-  
 495 ent melt parametrization are used in the interior and edges of large ice structures (see Sec-  
 496 tion 2.5). Figure 11 shows what the melt rates look like when using (a) the 3-equation-  
 497 model parametrization [Holland and Jenkins , 1999], (b) point-particle-iceberg-melt parametriza-  
 498 tion [Gladstone et al , 2001], and (c) the mixed-melt-rate parametrization (from Section  
 499 2.5). The 3-equation-model melt rates (Figure 11a) are about half the size of those calcu-  
 500 lated using the point-particle-iceberg-melt parametrization (Figure 11b). When the mixed-  
 501 melt-rate parametrization is used (Figure 11c), the very high melt rates are only observed  
 502 at the edges of ice structures. However, somewhat elevated melt rates at the steep ice  
 503 cliffs are still seen in the simulation using the 3-equation-model parametrization (Figure  
 504 11a), indicating these are not solely caused by our choice of parameterizations, but rather  
 505 there is an underlying dynamical mechanism causing elevated melt rates close to the steep  
 506 ice fronts.

## 507 5 Summary

508 In this study we present a novel framework for representing tabular icebergs in nu-  
 509 matical ocean models. In this framework, large tabular icebergs are constructed from col-  
 510 lections of Lagrangian elements that are held together by numerical bonds. Constructing  
 511 tabular icebergs out of many independent elements allows the icebergs to interact with  
 512 the ocean across a wide area (larger than a grid cell), and behave as if they had a finite  
 513 size and structure. This is in contrast to previous representations of icebergs in numerical  
 514 models [Jongma et al , 2009; Martin and Adcroft , 2010; Marsh et al , 2015] that repre-  
 515 sent icebergs as point particles. Explicitly resolving tabular icebergs in the ocean allows  
 516 the icebergs to interact with the ocean in a more realistic way, and allows us to study the  
 517 effect that tabular icebergs have on the ocean circulation. Including numerical bonds be-  
 518 tween elements allows for the possibility of breaking bonds to simulation iceberg calving  
 519 and fracture.

The capabilities of the tabular iceberg model were demonstrated by modeling a tabular iceberg drifting away from an idealized ice shelf (also constructed using Lagrangian elements). The results show that explicitly resolving the iceberg in the ocean allowed for a complex interaction between the tabular iceberg and the surrounding ocean. In our setup, the tabular iceberg is driven away from the ice shelf by ocean currents, wind stress, and the Coriolis force. As the iceberg moves through the water, it disturbs the ocean surface, driving ocean currents. The motion of the iceberg and melt beneath the iceberg drive upwelling along the sides of the iceberg, which entrains ambient water and causes a warming of the surface ocean in the wake of the iceberg. The changing ocean conditions feed back onto the iceberg, affecting its motion and melt rates. The highest melt rates are observed at edge of the iceberg which has the steepest ice cliff. These have the effect of smoothing out the ice edge over time. Simulations without using numerical bonds showed that these bonds are essential for allowing the iceberg to move as a unit. We also demonstrate that by breaking these numerical bonds we can simulate iceberg fracture, which is important process that increases the rate of iceberg decay.

To our knowledge, the model presented in this study is the first model to explicitly resolve drifting tabular icebergs in an ocean model that can be used for climate. A natural extension of this work is to try to include tabular icebergs into a general circulation model (GCM) used for climate projections. However, before this can be done, there are a number of issues that need to be resolved: firstly, the question of how and when to introduce tabular icebergs into the ocean needs to be addressed. For GCM's with active ice shelves, a calving law is needed to decide when to release the tabular iceberg into the ocean. The question of what calving law to use is a topic of ongoing research [Benn et all , 2007; Alley et al , 2008; Levermann et al , 2012; Bassis and Jacobs , 2013] and is still unresolved. One potential way to temporarily bypass this problem would be to run hindcast simulations using historically observed calving events. A related issue is the question of how and when to break the bonds within the freely floating icebergs to simulation iceberg breakup. Without a rule for iceberg breakup, the tabular icebergs would likely drift to unrealistically low latitudes. Another challenge will to develop methods to initialize the size and positions of elements on a spherical grid. This study used a cartesian coordinate system, which allowed us to initialize the ice elements in a regular staggered lattice. A different initialization method will be needed to generalize this initialization procedure to curved coordinates which are needed for large-scale global simulations. Further work is also needed to understand (and model) the interactions between tabular icebergs and sea ice, and to parametrize the effects of iceberg grounding, as these interactions play a large role in dictating the trajectories of tabular icebergs. However, despite these remaining challenges, the technical framework described in this article is potentially a using step towards including tabular icebergs in global GCM's, and hence a step towards making more accurate projections of future sea level.

## 6 Appendix A

### 6.1 Environmental forces on ice elements

The non-interactive forces on an ice element are as described in [Martin and Adcroft , 2010], and are repeated here for completeness. The forces on an element due to air (a), ocean (o) and sea ice (si) drag are given by

$$(\vec{F}_a) = \rho_a(0.5c_{a,v}WF + c_{a,h}LW)|\vec{u}_a - \vec{u}|(\vec{u}_a - \vec{u}), \quad (11)$$

$$(\vec{F}_o) = \rho_o(0.5c_{o,v}W(D - T_{si})F + c_{o,h}LW)|\vec{u}_o - \vec{u}|(\vec{u}_o - \vec{u}), \quad (12)$$

$$(\vec{F}_{si}) = \rho_{si}(0.5c_{si,v}WT_{si}F + c_{si,h}LW)|\vec{u}_{si} - \vec{u}|(\vec{u}_{si} - \vec{u}). \quad (13)$$

Here  $\rho_a$ ,  $\rho_o$ ,  $\rho_{si}$ , are the density of air, ocean and sea ice, respectively.  $c_{a,v}$ ,  $c_{o,v}$  and  $c_{si,v}$  are the vertical drag coefficients with air, ocean and sea ice, while  $c_{a,h}$ ,  $c_{o,h}$  and  $c_{si,h}$  are the respective horizontal drag coefficients.  $\vec{u}_a$ ,  $\vec{u}_o$ ,  $\vec{u}_{si}$ , are the velocities air,

569 ocean and sea ice, respectively. L, W, T, F and D are the length, width, thickness, free-  
 570 board and draft of the ice element. The element thickness is related to the draft and free-  
 571 board by  $T = F + D$  and  $D = \frac{\rho}{\rho_o}T$ , where  $\rho$  is the ice element density.  $T_{si}$  is the sea ice  
 572 thickness.

573 The wave radiation force ( $\vec{F}_R$ ) is given by

$$\vec{F}_R = \frac{1}{2}\rho_o c_r g a \min(a, F) 2 \frac{WL}{W+L} \frac{\vec{v}_a}{|\vec{v}_a|} \quad (14)$$

574 where g is the acceleration due to gravity, a is the wave amplitude empirically related to  
 575 the wind speed by  $a = 0.010125|\vec{v}_a - \vec{v}_o|$ , and  $c_{wd}$  is the wave drag coefficient defined as

$$c_{wd} = 0.06 \min\left(\max\left[0, \frac{L - L_c}{L_t - L_c}\right], 1\right), \quad (15)$$

576 where  $L_w = 0.32|\vec{v}_a - \vec{v}_o|^2$  is an empirical wave length,  $L_c = 0.125L_w$  is the cutoff length,  
 577 and  $L_t = 0.25L_w$  is the upper limit.

578 The pressure gradient force is approximated as a force due to sea surface slope and  
 579 given by

$$\vec{F}_{SS} = -Mg\vec{\nabla}\eta \quad (16)$$

580 where  $\eta$  is the sea surface height.

## 581 6.2 Melt rate parametrization

582 As discussed in Section 2.5, unbounded ice elements in the LBIM decay according  
 583 to parameterizations for iceberg decay typically used in iceberg drift models [Martin and  
 584 Adcroft , 2010], while ice elements within larger ice structures have only a basal melt  
 585 given by the three equation model [Holland and Jenkins , 1999] .

586 For unbonded ice elements, the element thickness decays due to basal melt at a rate  
 587  $M_b$ , while the length and width of the elements decay as a result of melt due to wave ero-  
 588 sion,  $M_e$ , and melt due to buoyant convection,  $M_v$ . Following Gladstone et al [2001] and  
 589 Martin and Adcroft [2010], the basal melt rate, wave erosion melt rate, and buoyant con-  
 590 vection melt rate are parameterized by

$$M_b = 0.58|\vec{v} - \vec{v}_0|^{0.8} \frac{\tilde{T}_0 - \tilde{T}}{L^{0.2}} \quad (17)$$

$$M_e = \frac{1}{12}S_s \left(1 + \cos[\pi A_i^3]\right) \left(\tilde{T}_0 + 2\right), \quad (18)$$

$$M_v = \left(7.62 \times 10^{-3}\right)\tilde{T}_0 + \left(1.29 \times 10^{-3}\right)\tilde{T}_0^2. \quad (19)$$

593  $\tilde{T}$  is the effective iceberg temperature and is set to  $\tilde{T} = 4^\circ\text{C}$ ,  $\tilde{T}_0$  is the temperature at the  
 594 top of the ocean,  $A_i$  is the sea ice area fraction, and  $S_s$  is the sea state, which is given by  
 595 the Beaufort scale

$$S_s = \frac{2}{3}|\vec{u}_a - \vec{u}_o|^{\frac{1}{2}} + \frac{1}{10}|\vec{u}_a - \vec{u}_o| \quad (20)$$

596 All three melt rates are in units of meters per day.

597 For elements inside larger structures, the melt due to wave erosion and melt due to  
 598 buoyant convection are set to zero, and the basal melt,  $M_s$  is given by the standard three  
 599 equation model [Holland and Jenkins , 1999].

## 600 7 Appendix B

### 601 7.1 Modified Verlet Algorithm

602 The LBIM uses a version velocity Verlet time-stepping algorithm, which has been  
 603 modified to allow part of the forcing to be calculated implicitly. The traditional velocity  
 604 Verlet algorithm is commonly used in molecular dynamics, as it is simple to implement,  
 605 second order accurate and computationally efficient [Swope et al , 1982; Omelyan et al ,  
 606 2002]. Here we modify the traditional scheme to allow for the drag forces to be modeled  
 607 implicitly, which prevents large accelerations for element's whose mass approaches zero.  
 608 To do this, we include both an implicit and explicit acceleration,  $a = a^{exp} + a^{imp}$ . The  
 609 explicit acceleration,  $a^{exp}$  includes all forcing terms which depend only on the previous  
 610 time step and the current position, while the implicit acceleration,  $a^{imp}$  includes forcing  
 611 terms which depend on the velocity at the current time step (in particular the drag and  
 612 Coriolis forces).

613 Using a time step of  $\Delta t$ , and subscripts to denote the time step (so that  $t_{n+1} = t_n +$   
 614  $\Delta t$ ), the modified velocity Verlet scheme can be written as:

- 615 1)  $x_{n+1} = x_n + u_n \Delta t + \frac{1}{2} \Delta t^2 \left( a_n^{exp} + a_n^{imp} \right).$
- 616 2) Calculate  $a_{n+1}^{exp}$
- 617 3) Calculate  $a_{n+1}^{imp}$  and  $u_{n+1} = u_n + \frac{\Delta t}{2} \left( a_n^{exp} + a_{n+1}^{exp} \right) + (\Delta t) a_{n+1}^{imp}$

618 This scheme reduces to the traditional velocity Verlet when  $a^{imp}$  is set to zero.  
 619 Note that  $a_{n+1}^{exp} = a_{n+1}^{exp}(x_{n+1}, t_n)$  is an explicit function of  $x_{n+1}$  and other quantities  
 620 evaluated at time  $t_n$ , while  $a_{n+1}^{imp} = a_{n+1}^{imp}(u_{n+1}, x_{n+1}, t_n)$  additionally depends on  $u_{n+1}$ ,  
 621 and needs to be solved implicitly. For this reason in step three,  $a_{n+1}^{imp}$  and  $u_{n+1}$  need to be  
 622 solved simultaneously, as described in the next subsection.

623 In equation (1), the forces due to ocean drag, atmospheric drag and sea ice drag are  
 624 treated implicitly. The force due to sea surface slope and wave radiation are treated ex-  
 625 plicitly. The Coriolis term is handled using Crank-Nicolson scheme so that half of the  
 626 effect is implicit and half is explicit. The elastic part of the interactive forces is treated ex-  
 627 plicitly, while the interactive damping is handled semi-implicitly in that the drag force on  
 628 element A by element B depends on the velocities of elements A and B evaluated at time  
 629  $t_{n+1}$  and  $t_n$ , respectively.

### 630 7.2 Solving for the velocity implicitly

631 Since this modified scheme contains some forcing terms which are handled im-  
 632 plicitly,  $a_{n+1}^{imp}$  and  $u_{n+1}$  need to be calculated simultaneously. We demonstrate how this  
 633 is done, using a simplified one-dimensional version of equation (1), neglecting the atmo-  
 634 spheric drag, sea ice drag and Coriolis force, so that the only implicitly treated term is the  
 635 ocean drag. In this demonstration, we use a superscript to denote the ocean drag force,  
 636  $F^o$ , and ocean velocity,  $u^o$ , to avoid confusion with the subscripts indicating time step.  
 637 We also define an explicit force,  $F^{exp}$ , which accounts for all forces not proportional the  
 638 element velocity. With these simplifications, the implicit and explicit accelerations are

$$639 a^{exp} = \frac{1}{M} (\vec{F}^{exp}) \quad (21)$$

$$a^{imp} = \frac{1}{M} (F^o) \quad (22)$$

640 The ocean drag force at time  $t_{n+1}$  is modeled (mostly) implicitly as

$$F_{n+1}^o = \tilde{c}^o |u_n^o - u_n| (u_n^o - u_{n+1}), \quad (23)$$

641 where  $\tilde{c}^o$  is the effective drag coefficient, accounting for the dimensions of the ice element  
 642 (see equation 12).

643 Step 3 of the modified velocity Verlet scheme can be rewritten by introducing an  
 644 intermediate velocity  $u^*$ , which only depends on the velocity and acceleration at time  $t_n$ ,

$$u_n^* = u_n + \frac{1}{2}(\Delta t)a_n^{exp}. \quad (24)$$

645 Using this, the updated velocity (Step 3) can be written

$$u_{n+1} = u_n^* + \frac{\Delta t}{2}a_{n+1}^{exp} + (\Delta t)a_{n+1}^{imp}. \quad (25)$$

646 Including the forcing terms into this equations gives

$$u_{n+1} = u_n^* + \frac{\Delta t}{2M}(F_{n+1}^{exp}) + \frac{\Delta t}{M}\left(c_w|u_n^o - u_n|(u_n^o - u_{n+1})\right) \quad (26)$$

647 Solving for  $u(t_{n+1})$  in terms of quantities which only depend on the previous time step  
 648 gives

$$u_{n+1} = \frac{u_n^* + \frac{\Delta t}{2M}(F_{n+1}^{exp}) + \frac{\Delta t}{M}\left(c_w|u_n^o - u_n|(u_n^o - u_{n+1})\right)}{\left(1 + \frac{\Delta t}{M}c_w|u_n^o - u_n|\right)} \quad (27)$$

649 Once the  $u_{n+1}$  has been found, it can be used to calculate the explicit and implicit acceler-  
 650 ations, which are required for the next time step.

651 Finally, we note that the the drag term (equation 23) is not entirely implicit, since  
 652 the element velocity inside the absolute value is evaluated at time  $t_n$ , rather than at time  
 653  $t_{n+1}$ . This is done so that we can solve for the updated velocity analytically. One conse-  
 654 quence of this is that it can give rise to a small oscillation in the element velocity. This  
 655 oscillation is addressed by using a predictive corrective scheme: after solving for a first  
 656 guess of the velocity at time  $t_{n+1}$ , this estimate of the velocity is used to update the esti-  
 657 mate of the drag force (i.e.: inside the absolute value signs). This updated drag, can now  
 658 be used to repeat the process described above to find an improved estimate of the velocity.  
 659 We found that two iterations were sufficient to remove the unwanted oscillation.

660 The procedure described in this section is easily extended to include more forcing  
 661 terms and two dimensions (where it involves inverting a  $2 \times 2$  matrix).

## 662 8 Appendix C

### 663 Connecting bonds across processor boundaries

664 Since the LBIM is parallelized across multiple processors, it often happens that two  
 665 elements on different processes are bonded together. Keeping track of numerical bonds  
 666 across processor boundaries requires a lot of book keeping. In this section we describe the  
 667 how LBIM handles bonds across processor boundaries.

668 The basics of the bond bookkeeping work as follows: consider an element A and  
 669 an element B that are bonded together. Each element has a copy of the bond (a piece of  
 670 memory which describes the bond between the two elements), which is stored with the  
 671 element. Let A-B be the bond stored by element A, and B-A be the bond stored by ele-  
 672 ment B. Bond A-B contains a pointer which points to element B and bond B-A contains a  
 673 pointer which points to element A.

674 Consider a situation where element A and B are originally on Processor 1, and then  
 675 element B moves to Processor 2. When this occurs, the memory assigned to element B  
 676 on processor 1 is removed, and is allocated on Processor 2. This means that the pointer  
 677 to element B in bond A-B (stored in element A on Processor 1) is no longer assigned.  
 678 Similarly, the pointer to element A in bond B-A (stored in element B on Processor 2) is

no longer assigned. Before the next time step, a halo update occurs, so that there is a copy of element A in the halo of Processor 2 and a copy of element B in the halo of Processor 1. After the halo update, the bonds A-B and B-A have to be reconnected on both Processor 1 and 2. To aid in reconnecting the bonds, a copy of the grid cell number of element B is stored in the bond A-B and a copy of the grid cell number of element A is stored in the bond B-A. We refer to this as the ‘most recent address’. Before a bond is moved from one processor to another, the ‘most recent address’ is updated, so that the bond can be reconnected later. To reconnect bond A-B on Processor 1 (for example), we find the most recent address of element B, and search through the list of elements in the grid cell corresponding to the most recent address of element B until element B is found. The pointer to element B in bond A-B is reassigned, and the bond is said to be connected.

The reconnected bond A-B (stored in element A) is said to be working properly when the following four test pass:

1. The pointer to element B is assigned on bond A-B.
2. The corresponding bond B-A exists on element B.
3. A pointer to element A exists in this bond B-A.
4. The element A which is being pointed to is the same element A where you started.

A useful tool disconnecting and reconnecting bonds is that each element is assigned a unique number so that elements are easily identified.

698  
699

**Acknowledgments**

= enter acknowledgments here =

700 **References**

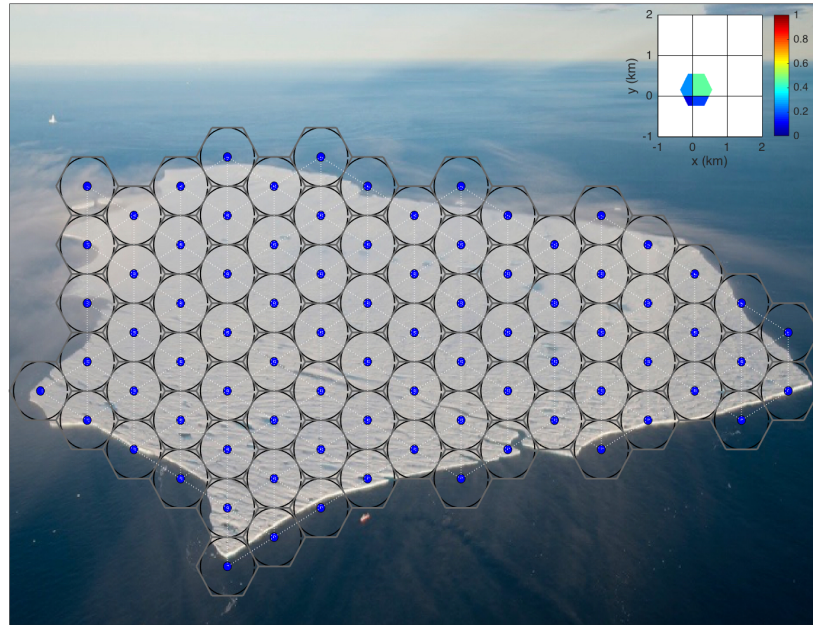
- 701 Asay-Davis, X. S., S. L. Cornford, B. K. Galton-Fenzi, R. M. Gladstone, G. H. Gud-  
 702 mundsson, D. M. Holland, P. R. Holland, and D. F. Martin (2016), Experimental de-  
 703 sign for three interrelated marine ice sheet and ocean model intercomparison projects:  
 704 MISMIP v. 3 (MISMIP+), ISOMIP v. 2 (ISOMIP+) and MISOMIP v. 1 (MISOMIP1).  
 705 *Geoscientific Model Development* 9, no. 7: 2471.
- 706 Arrigo, K. R., G. L. van Dijken, D. G. Ainley, M. A. Fahnestock, and T. Markus (2002).  
 707 Ecological impact of a large Antarctic iceberg. *Geophys. Res. Lett.*, 29(7).
- 708 Alley, R. B., H. J. Horgan, I. Joughin, K. M. Cuffey, T. K. Dupont, B. R. Parizek, S.  
 709 Anandakrishnan, and J. Bassis (2008), A simple law for ice-shelf calving. *Science* 322,  
 710 no. 5906, 1344-1344.
- 711 Bassis, J. N., and S. Jacobs (2013), Diverse calving patterns linked to glacier geometry.  
 712 *Nature Geoscience*, 6(10), 833-836.
- 713 Benn, D. I., C. R. Warren, and R. H. Mottram (2007). Calving processes and the dynam-  
 714 ics of calving glaciers. *Earth-Science Reviews*, 82(3), 143-179.
- 715 Bigg, G. R., Wadley, M. R., Stevens, D. P., and Johnson, J. A. (1997), Modeling the dy-  
 716 namics and thermodynamics of icebergs. *Cold Regions Science and Technology*, 26(2),  
 717 113-135.
- 718 Borstad, C. P., A. Khazendar, E. Larour, M. Morlighem, E. Rignot, M. P. Schodlok, and  
 719 H. Seroussi (2012), A damage mechanics assessment of the Larsen B ice shelf prior to  
 720 collapse: Toward a physically-based calving law, *Geophys. Res. Lett.*, 39, L18502
- 721 Biddle, L. C., J. Kaiser, K. J. Heywood, A. F. Thompson and A. Jenkins (2015), Ocean  
 722 glider observations of iceberg-enhanced biological productivity in the northwestern  
 723 Weddell Sea, *Geophys. Res. Lett.*, 42, 459-465.
- 724 De Rydt, J., and G. H. Gudmundsson (2016), Coupled ice shelf ocean modeling and com-  
 725 plex grounding line retreat from a seabed ridge. *J. of Geophys. Res.: Earth Surface*,  
 726 121(5), 865-880.
- 727 Dunne, J.P., J.G. John,, A.J. Adcroft, S.M. Griffies, R.W. Hallberg, E. Shevliakova, R.J.  
 728 Stouffer, W. Cooke, K.A. Dunne, M.J Harrison, and J.P. Krasting (2012), GFDL's  
 729 ESM2 global coupled climate-carbon Earth System Models. Part I: Physical formula-  
 730 tion and baseline simulation characteristics. *J. of Climate*, 25(19), 6646-6665.
- 731 Depoorter, M. A., J. L. Bamber, J. A. Griggs, J. T. M. Lenaerts, Stefan RM Ligtenberg,  
 732 M. R. van den Broek, and G. Moholdt (2013), Calving fluxes and basal melt rates of  
 733 Antarctic ice shelves. *Nature*, 502(7469), 89-92.
- 734 Determan J., Gerdes R. (1994), Melting and freezing beneath ice shelves: implications  
 735 from a three-dimensional ocean-circulation model. *Ann. Glaciol.*, 20, 413-419.
- 736 Dowdeswell, J. A., and J. L. Bamber (2007), Keel depths of modern Antarctic icebergs  
 737 and implications for sea-floor scouring in the geological record. *Marine Geology*,  
 738 243(1), 120-131.
- 739 Duprat, L. P., G. R. Bigg, and D. J. Wilton (2016), Enhanced Southern Ocean marine pro-  
 740 ductivity due to fertilization by giant icebergs. *Nature Geoscience*.
- 741 Eckert, E. R. G. (1950). Introduction to the Transfer of Heat and Mass. McGraw-Hill.
- 742 Fogwill, C.J., E. van Sebille, E.A. Cougnon, C.S. Turney, S.R. Rintoul, B.K. Galton-Fenzi,  
 743 G.F. Clark, E.M. Marzinelli, E.B. Rainsley, and L. Carter (2016), Brief communication:  
 744 Impacts of a developing polynya off Commonwealth Bay, East Antarctica, triggered by  
 745 grounding of iceberg B09B. *The Cryosphere*, 10(6), p.2603.
- 746 Gladstone, R. M., G. R. Bigg, and K. W. Nicholls. (2001), Iceberg trajectory model-  
 747 ing and meltwater injection in the Southern Ocean (1978-2012). *J. of Geophys. Res.:*  
 748 *Oceans*, 106(C9), 19903-19915.
- 749 Goldberg, D. N., C. M. Little, O. V. Sergienko, A. Gnanadesikan, R. Hallberg, and M.  
 750 Oppenheimer (2012), Investigation of land ice/ocean interaction with a fully coupled  
 751 ice-ocean model: 1. Model description and behavior. *J. of Geophys. Res.: Earth Surface*,  
 752 117(F2).

- 753 Gladish, C. V., D. M. Holland, P. R. Holland, and S. F. Price (2012), Ice-shelf basal chan-  
754 nels in a coupled ice/ocean model. *J. of Glaciol.*, 58(212), 1227-1244.
- 755 Grosfeld K., R. Gerdes, J. Determan (1997), Thermohaline circulation and interaction  
756 between ice shelf cavities and the adjacent open ocean. *J. Phys. Oceanogr.*, **102**, C7,  
757 15959-15610.
- 758 Grosfeld, K., and H. SandhŁger, (2004). The evolution of a coupled ice shelfDocean sys-  
759 tem under different climate states. *Global and Planetary Change*, 42(1), 107-132.
- 760 Hallberg, R., A. Adcroft, J. P. Dunne, J. P., Krasting, R. J., and Stouffer (2013), Sensitiv-  
761 ity of twenty-first-century global-mean steric sea level rise to ocean model formulation.  
762 *J. of Climate*, 26(9), 2947-2956.
- 763 Holland D. M., Jenkins A. (2001), Adaptation of an isopycnic coordinate ocean model for  
764 the study of circulation beneath ice shelves. *Mon. Wea. Rev.*, 129, 1905-1927.
- 765 Holland P. R. and D. L. Feltham (2006), The effects of rotation and ice shelf topography  
766 on frazil-laden Ice Shelf Water plumes. *J. Phys. Oceanogr.*, 36, 2312-2327.
- 767 Holland, D. M., and A. Jenkins (1999), Modeling thermodynamic ice-ocean interactions at  
768 the base of an ice shelf. *J. of Phys. Oceanogr.* 29.8, 1787-1800.
- 769 Hellmer H.H., Olbers D. J. (1989), A two-dimensional model for the thermohaline circula-  
770 tion under an ice shelf. *Antarctic Science*, 1, 325- 336.
- 771 Henderson J., J. S. P. Loe (2016), The Prospects andChallenges for Arctic Oil Develop-  
772 ment. *Oil, Gas and Energy Law Journal (OGEL)*, 14 (2)
- 773 Hopkins, M. A. (1996). On the mesoscale interaction of lead ice and floes. *J. of Geophys.  
Res.: Oceans*, 101(C8), 18315-18326.
- 774 Gaskill, H. S., and J. Rochester (1984). A new technique for iceberg drift prediction. *Cold  
Reg. Sci. Technol.*, 8(3), 223-234.
- 775 Jakobsen, T. (2001). Advanced character physics. In *Game Developers Conference*, Vol. 3.
- 776 Jenkins, A., P. Dutrieux, S. S. Jacobs, S. D. McPhail, J. R. Perrett, A. T. Webb, and D.  
777 White (2010), Observations beneath Pine Island Glacier in West Antarctica and implica-  
778 tions for its retreat. *it Nature Geo.*, 3(7), 468-472.
- 779 Jacobs, S. S., A. Jenkins, C. F. Giulivi, and P. Dutrieux (2011). Stronger ocean circulation  
780 and increased melting under Pine Island Glacier ice shelf. *Nature Geo.*, 4(8), 519-523.
- 781 Jongma, J. I., E. Driesschaert, T. Fichefet, H. Goosse, and H. Renssen (2009), The ef-  
782 fect of dynamic-thermodynamic icebergs on the Southern Ocean climate in a three-  
783 dimensional model, *Ocean Modell.*, 26, 104D113.
- 784 Kubat I., M. Sayed, S. Savage, T. Carrières (2005), An operational model of iceberg drift  
785 *Int. J. Off. Polar Eng.*, 15 (2), 125D131
- 786 Lewis E.L. and R.G. Perkin (1986), Ice pumps and their rates. *J. of Geophys. Res.*, 91,  
787 11756-11762.
- 788 Losch, M. (2008). Modeling ice shelf cavities in a z coordinate ocean general circulation  
789 model. *J. of Geophys. Res.: Oceans*, 113(C8).
- 790 Li, B., H. Li, Y. Liu, A. Wang and S. Ji (2014), A modified discrete element model for  
791 sea ice dynamics. *Acta Oceanologica Sinica*, 33(1), 56-63.
- 792 Liu, M. B. and G. R. Liu (2010), Smoothed particle hydrodynamics (SPH): an overview  
793 and recent developments. *Archives of computational methods in engineering*, 17(1), 25-  
794 76.
- 795 Lichéy, C., and H. H. Hellmer (2001). Modeling giant-iceberg drift under the influence of  
796 sea ice in the Weddell Sea, Antarctica. *J. of Glaciol.*, 47(158), 452-460.
- 797 Levermann, A., T. Albrecht, R. Winkelmann, M. A. Martin, M. Haseloff, and I. Joughin.  
798 (2012), Kinematic first-order calving law implies potential for abrupt ice-shelf retreat.  
799 *The Cryosphere*, 6(2), 273-286.
- 800 Mountain, D. G. (1980). On predicting iceberg drift. *Cold Reg. Sci. Technol.*, 1(3-4), 273-  
801 282.
- 802 Martin, T., and Adcroft, A. (2010), Parameterizing the fresh-water flux from land ice to  
803 ocean with interactive icebergs in a coupled climate model. *Ocean Modelling*, 34(3),

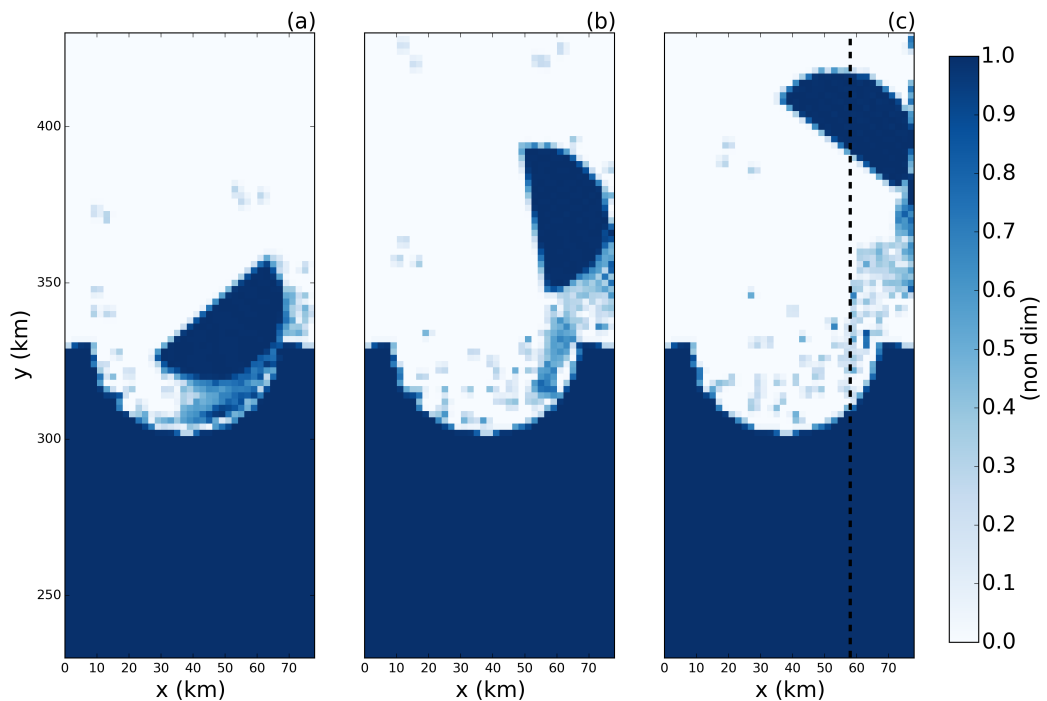
- 806 111-124.
- 807 Marsh, R., V. O. Ivchenko, N. Skliris, S. Alderson, G. R. Bigg, G. Madec, A. T. Blaker  
 808 Y. Aksenov, B. Sinha, A.C. Coward, and J.L. Sommer (2015), NEMO $\delta$ ICB (v1. 0):  
 809 interactive icebergs in the NEMO ocean model globally configured at eddy-permitting  
 810 resolution. *Geoscientific Model Development* 8, no. 5 (2015): 1547-1562.
- 811 MacAyeal D.R. (1984), Thermohaline Circulation Below the Ross Ice Shelf: A Conse-  
 812 quence of Tidally Induced Vertical Mixing and Basal Melting. *J. Geophys. Res.*, 89,  
 813 597-606
- 814 Merino, N., Le Sommer, J., Durand, G., Jourdain, N. C., Madec, G., Mathiot, P., and  
 815 Tournadre, J. (2016), Antarctic icebergs melt over the Southern Ocean: climatology and  
 816 impact on sea ice. *Ocean Modelling*, 104, 99-110.
- 817 Nicholls K.W. (1996), Temperature variability beneath Ronne Ice Shelf, Antarctica, from  
 818 thermistor cables. *J. Phys. Oceanogr.*, 11, 1199-1210.
- 819 Nicholls KW, Østerhus S, Makinson K (2009), Ice-Ocean processes over the continental  
 820 shelf of the southern Weddell Sea, Antarctica: a review. *Rev. Geophys.* 47(3).
- 821 Omelyan, I. P., M. I. Mryglod, and R. Folk (2002), Optimized Verlet-like algorithms for  
 822 molecular dynamics simulations. *Physical Review E*, 65(5), 056706.
- 823 Rignot, E., S. Jacobs, J. Mouginot, and B. Scheuchl (2013), Ice-shelf melting around  
 824 Antarctica. *Science*, 341, no. 6143 (2013): 266-270.
- 825 Robinson, N. J., M. J. M. Williams, P. J. Barrett, and A. R. Pyne (2010), Observations of  
 826 flow and ice-ocean interaction beneath the McMurdo Ice Shelf, Antarctica, *J. Geophys.*  
 827 *Res.*, 115, C03025
- 828 Pizzolato, L., S. E. Howell, C. Derksen, J. Dawson, L. Copland (2014), Changing sea ice  
 829 conditions and marine transportation activity in Canadian Arctic waters between 1990  
 830 and 2012, *Climatic Change* 123 (2), 161173.
- 831 Pan, W., A. M. Tartakovsky, and J. J. Monaghan (2013). Smoothed particle hydrodynam-  
 832 ics non-Newtonian model for ice-sheet and ice-shelf dynamics. *J. of Comp. Phys.*, 242,  
 833 828-842.
- 834 Pralong, A., and M. Funk (2005), Dynamic damage model of crevasse opening and appli-  
 835 cation to glacier calving, *J. Geophys. Res.*, 110, B01309.
- 836 Sergienko, O. V. (2013). Basal channels on ice shelves. *J. of Geophys. Res.: Earth Surface*,  
 837 118(3), 1342-1355.
- 838 Silva, T. A. M., Bigg, G. R., and Nicholls, K. W. (2006), Contribution of giant icebergs to  
 839 the Southern Ocean freshwater flux. *J. of Geophys. Res.: Oceans*, 111(C3).
- 840 Smith, K., B. Robison, J. Helly, R. Kaufmann, H. Ruhl, H., T. Shaw, and M. Vernet  
 841 (2007), Free-drifting icebergs: Hotspots of chemical and biological enrichment in the  
 842 Weddell Sea, *Science*, 317, 478-482.
- 843 Shepherd, A., and D. Wingham (2007). Recent sea-level contributions of the Antarctic and  
 844 Greenland ice sheets. *Science*, 315(5818), 1529-1532.
- 845 Stern, A. A., D. M. Holland, P. R. Holland, A. Jenkins and J. Sommeria (2014), The ef-  
 846 fect of geometry on ice shelf ocean cavity ventilation: a laboratory experiment. *Experi-  
 847 ments in Fluids*, 55(5), 1-19.
- 848 Stern, A.A., Johnson, E., Holland, D.M., Wagner, T.J., Wadhams, P., Bates, R., Abraham-  
 849 sen, E.P., Nicholls, K.W., Crawford, A., Gagnon, J. and Tremblay, J.E. (2015), Wind-  
 850 driven upwelling around grounded tabular icebergs. *J. of Geophys. Res.: Oceans*, 120(8),  
 851 5820-5835.
- 852 Stern, A. A., A. Adcroft, and O. Sergienko (2016), The effects of Antarctic iceberg calv-  
 853 ing size distribution in a global climate model. *J. of Geophys. Res.: Oceans*, 121(8),  
 854 5773-5788.
- 855 Swope, W. C., H. C. Andersen, P. H. Berens, and K. R. Wilson (1982), A computer sim-  
 856 ulation method for the calculation of equilibrium constants for the formation of physi-  
 857 cal clusters of molecules: Application to small water clusters. *The Journal of Chemical*  
 858 *Physics* 76, no. 1, 637-649.

- 859 Tournadre, J., N. Bouhier, F. Girard-Ardhuin, and F. RÖmy (2016), Antarctic icebergs dis-  
860 tributions 1992-2014. *J. Geophys Res: Oceans*.
- 861 Turnbull I.D., N. Fournier, M. Stolwijk, T. Fosnaes, D. McGonigal (2015), Operational  
862 iceberg drift forecasting in Northwest Greenland, *Cold Reg. Sci. Technol.* 110, 1-18
- 863 Unger, J. D., 2014. Regulating the Arctic Gold Rush: Recommended Regulatory Reforms  
864 to Protect Alaska's Arctic Environment from Offshore Oil Drilling Pollution . *Alaska L.*  
865 *Rev*, 31
- 866 Vernet, M., et al. (2012), Islands of ice: Influence of free-drifting Antarctic icebergs on  
867 pelagic marine ecosystems, *Oceanography*, 25(3), 38Ð39
- 868 Wagner, T. J., Wadhams, P., Bates, R., Elosegui, P., Stern, A., Vella, D., E. P. Abraham-  
869 sen, A. Crawford, and Nicholls, K. W. (2014), The ÒfootlooseÓ mechanism: Iceberg  
870 decay from hydrostatic stresses. *Geophys. Res. Lett.*, 41(15), 5522-5529.
- 871 Weeks, W. F., and W. J. Campbell (1973). Icebergs as a fresh-water source: an appraisal.  
872 *J. of Glaciol.*, 12(65), 207-233.
- 873 White, L., A. Adcroft, and R. Hallberg (2009), High-order regridding-remapping schemes  
874 for continuous isopycnal and generalized coordinates in ocean models. *J. of Comp.*  
875 *Phys.*, 228(23), 8665-8692.

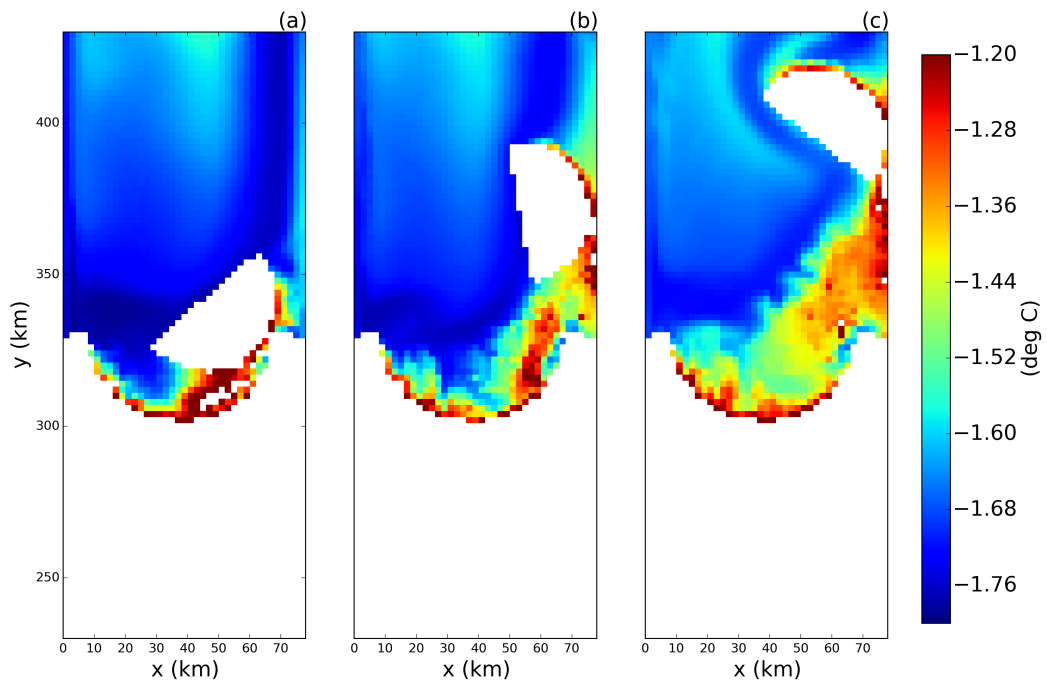
Parameter	Symbol	Value	Unit
Domain Length	$L_x$	80	km
Domain Width	$L_y$	480	km
Horizontal Resolution	$\Delta x$	2	km
Number of vertical layers	$N_l$	72	non-dim
Horizontal Viscosity	$\nu_H$	6.0	$\frac{m^2}{s}$
Diapycnal Viscosity	$\nu_V$	$10^{-3}$	$\frac{m}{s}$
Horizontal Diffusivity	$\epsilon_H$	1.0	$\frac{m^2}{s}$
Diapycnal Diffusivity	$\epsilon_V$	$5 \times 10^{-5}$	$\frac{m^2}{s}$
Initial Surface Temperature	$T_t$	-1.9	°C
Initial Bottom Temperature	$T_b$	1.0	°C
Initial Surface Salinity	$S_t$	33.8	psu
Initial Bottom Salinity	$S_b$	34.7	psu
Maximum Ocean depth	$H_{ocean}$	720	m
Relaxation Time of Sponge Layer	$T_{sponge}$	0.1	days
Time Step for Static Shelf Experiment	$dt_{Static}$	1000	s
Time Step for Iceberg Calving Experiment	$dt_{Calving}$	10	s



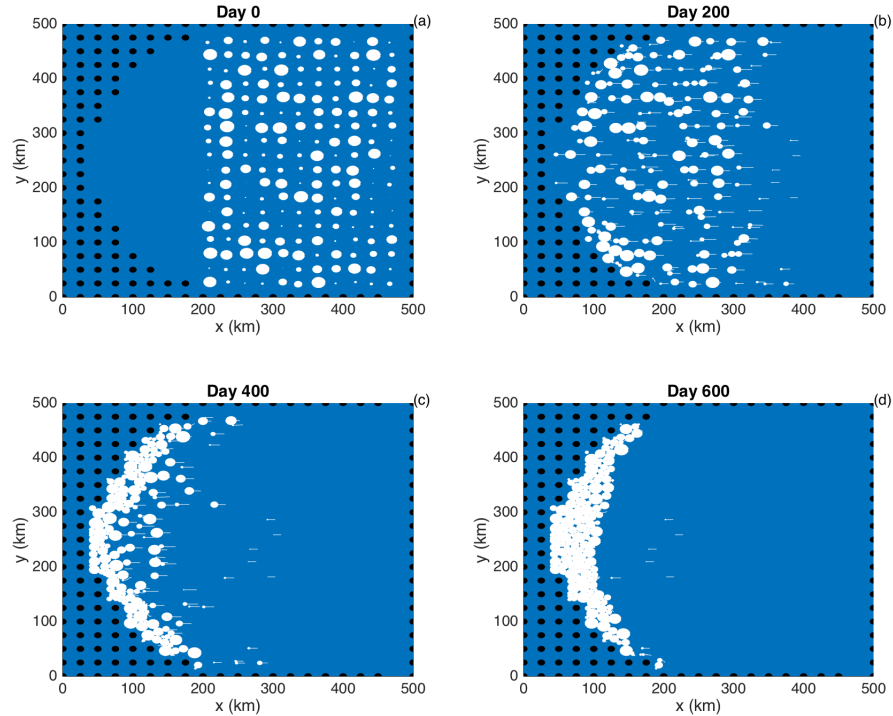
876 **Figure 1.** Schematic showing how Lagrangian elements are used when modeling tabular icebergs. La-  
 877 grangian elements (blue dots) are initialized in a staggered lattice covering the surface area of the iceberg.  
 878 For purposes of mass aggregation, the ice elements are assumed to have hexagonal shape (grey hexagons).  
 879 For purposes of element interactions, the ice elements are assumed to be circular (black circles). Elements  
 880 are initially bonded to adjacent elements using numerical bonds (dashed white lines). These numerical bonds  
 881 form equilateral triangles which give the shape rigidity. The inset panel shows a schematic of the intersection  
 882 of a hexagonal element and the ocean grid. The colors indicate the fraction of the hexagon that lies in each  
 883 grid cell. These fractions are used as weights to spread LBIM properties to the ocean grid (see text for more  
 884 details) The background photo in the larger schematic is an areal photograph of iceberg PIIB (Area= 42 km<sup>2</sup>)  
 885 taken in Baffin Bay in 2012. The red ship can be identified on the bottom of the photo for scale.



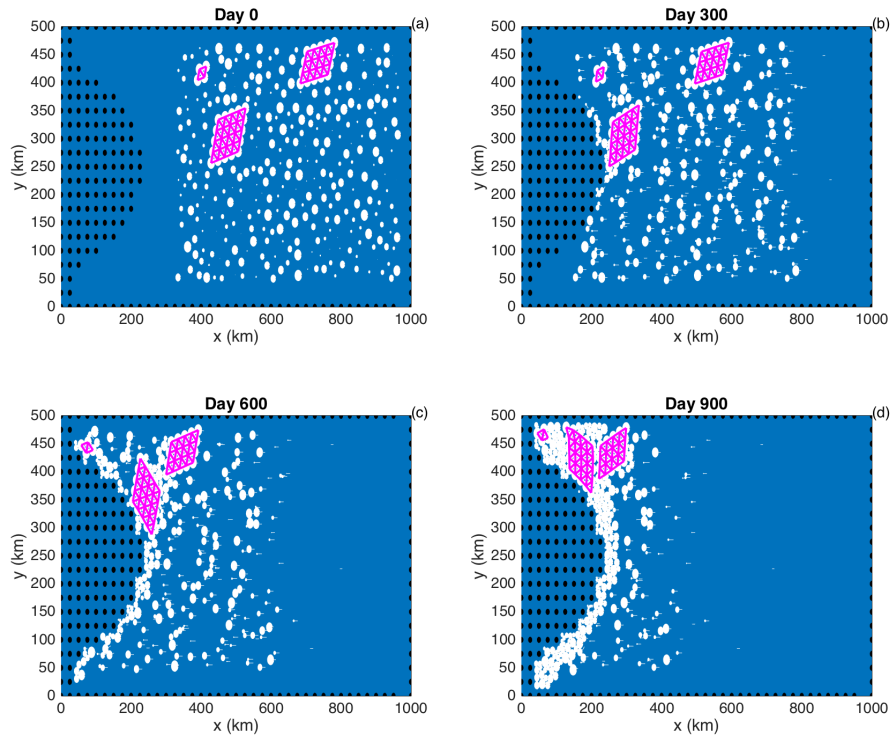
886 **Figure 2.** Snapshots of the fraction of ice cover in the LBIM tabular iceberg calving simulation. Snapshots  
887 are taken (a) 7, (b) 15, and (c) 30 days after calving. The dashed line in panel (c) shows the location of the  
888 vertical transects shown in Figures 8 and 7.



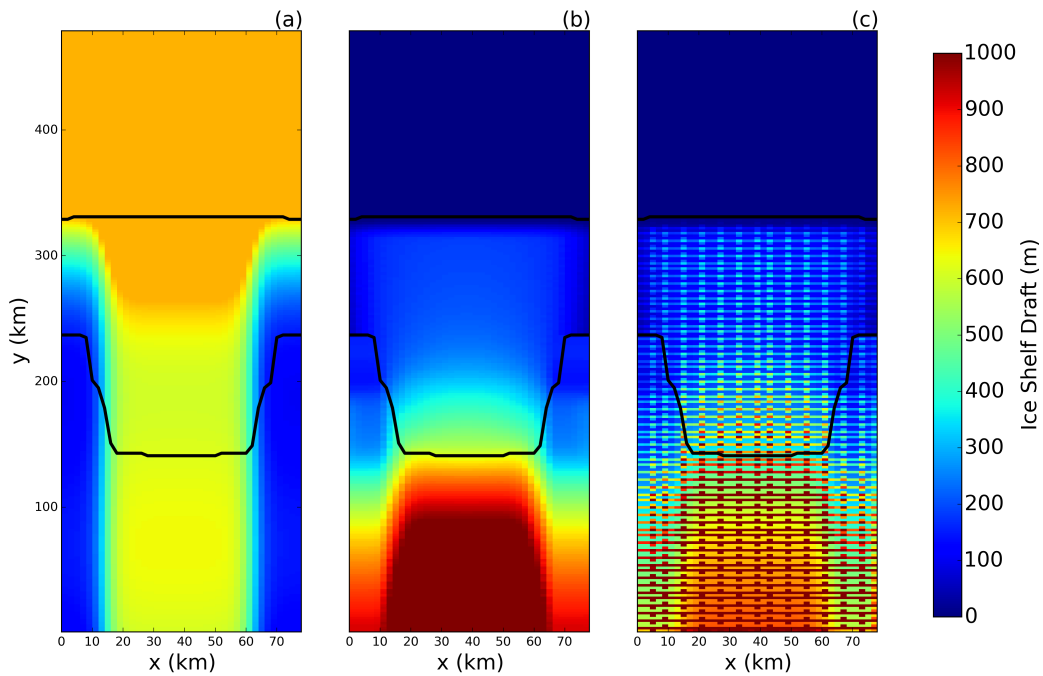
889 **Figure 3.** Snapshots of the sea surface temperature in the LBIM tabular iceberg calving simulation. Snap-  
890 shots are taken (a) 7, (b) 15, and (c) 30 days after calving. Regions with ice area fraction = 1 area plotted in  
891 white.



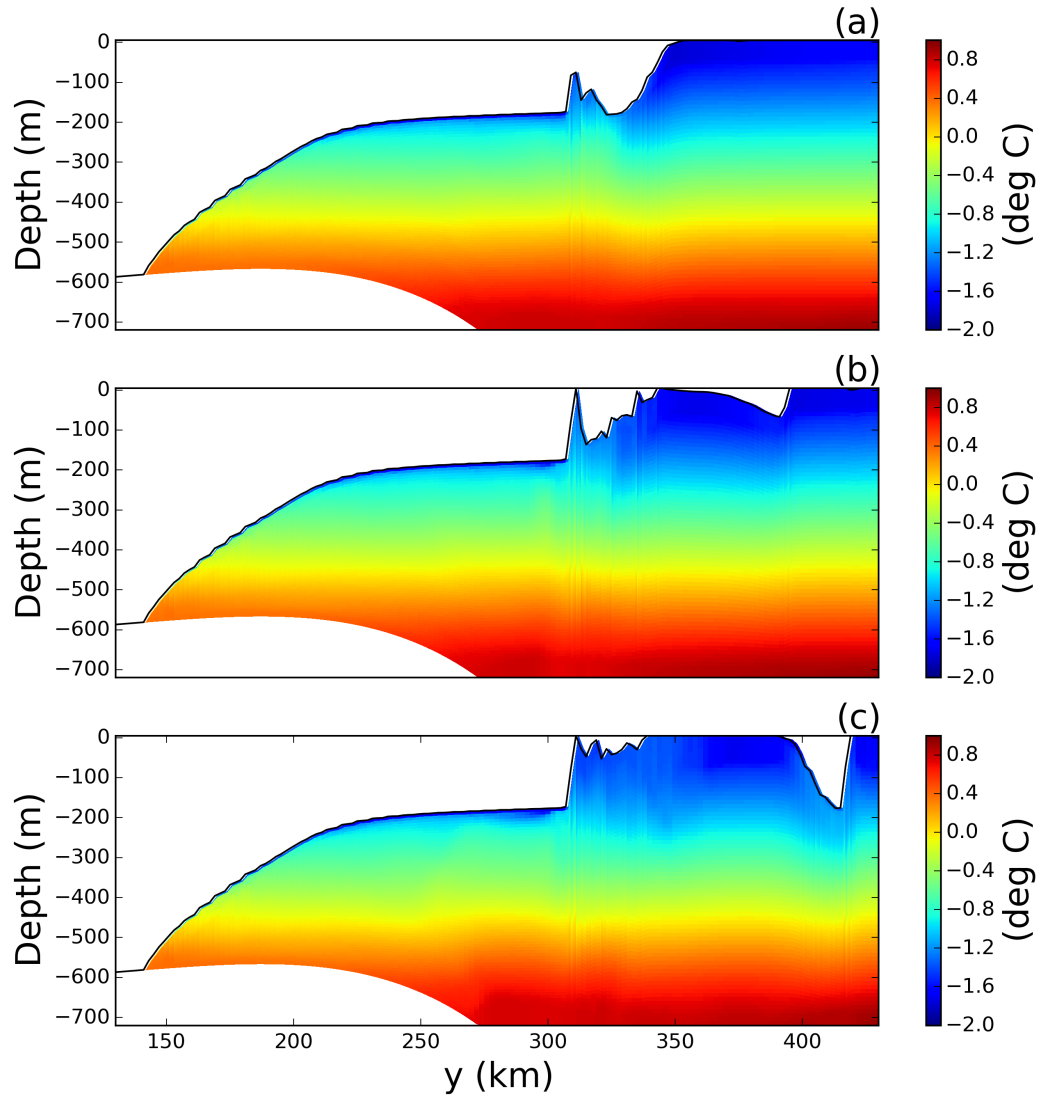
892 **Figure 4.** Results of an ice-only LBIM simulation with no bonds between ice elements. Ice elements are  
 893 initialized throughout the domain, as shown in panel (a). The elements are forced by an imposed westward  
 894 ocean current of  $u=0.1\text{m/s}$  (no ocean model is used). Forces due to sea surface slope, atmospheric drag, Cori-  
 895 olis and sea ice drag are set to zero. The figure shows snapshots of ice element positions at time (a)  $t=0$ , (b)  
 896 200, (c) 400, (d) 600 days. The size of the dots shows the surface area (and interaction diameter) of each ice  
 897 element. The white tails behind the elements show the elements' positions over the preceding two days. Land  
 898 points are shown by black circles.



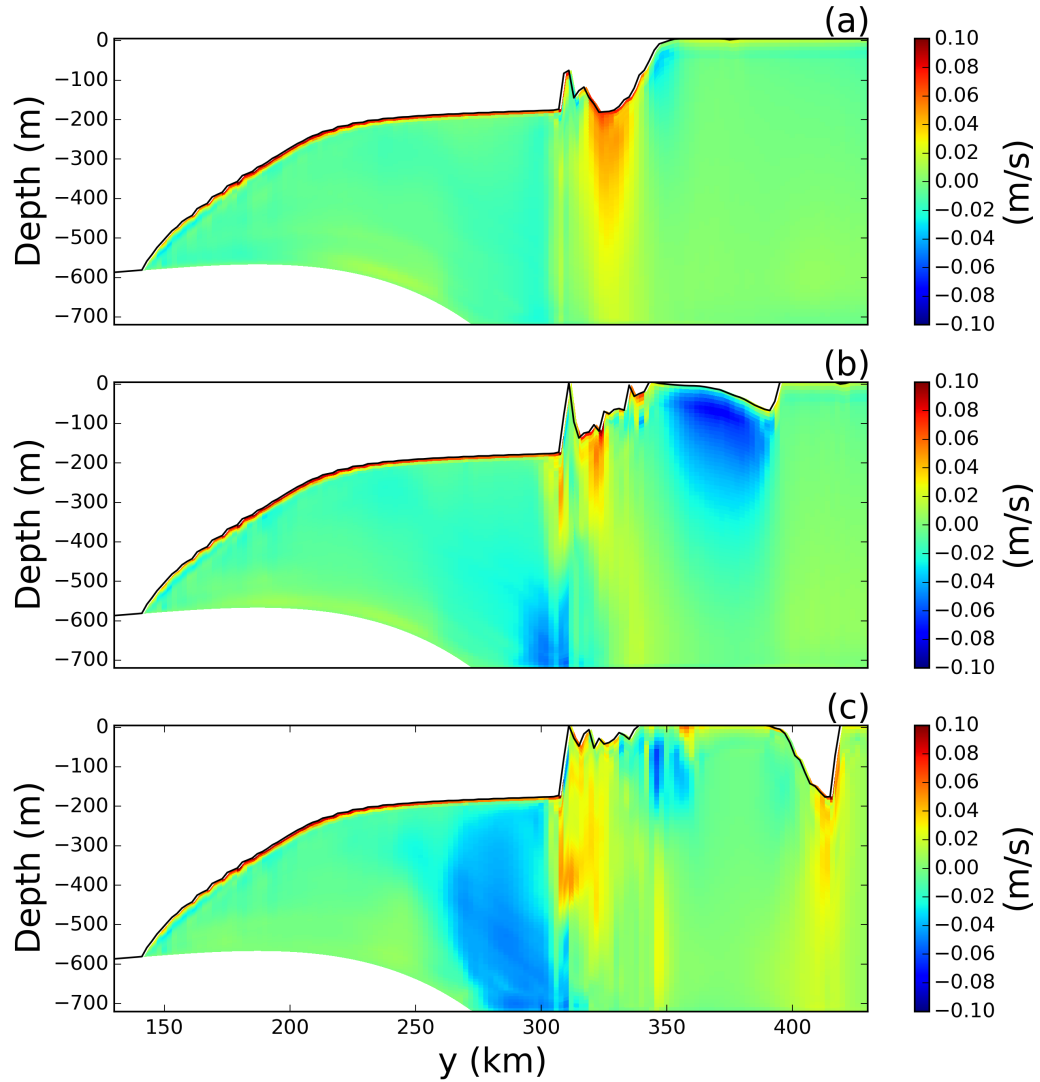
899 **Figure 5.** Results of an ice-only LBIM simulation using bonds between elements. Ice elements are ini-  
 900 tialized throughout the domain, as shown in panel (a). Three tabular icebergs are included, with 25, 16 and 4  
 901 elements respectively. The elements are forced by an imposed westward ocean current of  $u=0.1\text{m/s}$  (no ocean  
 902 model is used). Forces due to sea surface slope, atmospheric drag, Coriolis and sea ice drag are set to zero.  
 903 The figure shows snapshots of ice element positions at time (a)  $t=0$ , (b) 300, (c) 600, (d) 900 days. The size  
 904 of the dots shows the surface area (and interaction diameter) of each ice element. The white tails behind the  
 905 elements show the elements' positions over the preceding two days. Bonds between ice elements are plotted  
 906 in magenta. Land points are shown by black circles.



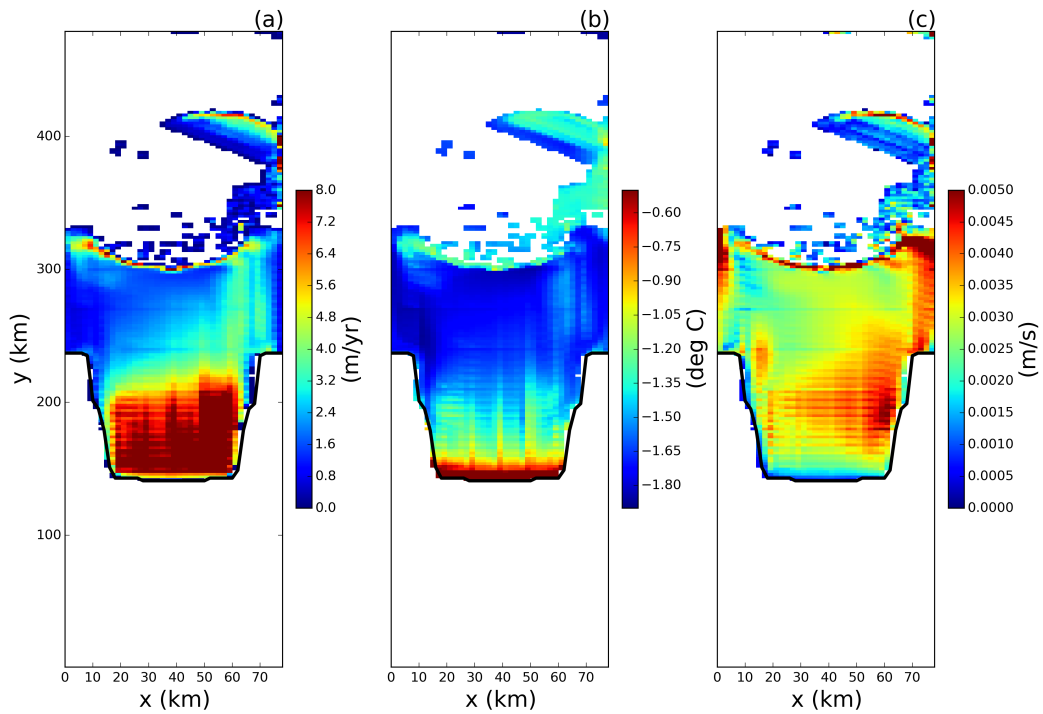
907      **Figure 6.** (a) Ocean bottom topography and (b) ice-shelf draft used to initialize the tabular iceberg calv-  
908      ing simulation. The ice draft is calculated from the total mass in an ocean grid cell after the mass-spreading  
909      interpolation has been applied (as explained in Section 2.3). (c) Initial ice draft that would be calculated if the  
910      mass-spreading interpolation were not used (i.e.: elements treated as point masses).



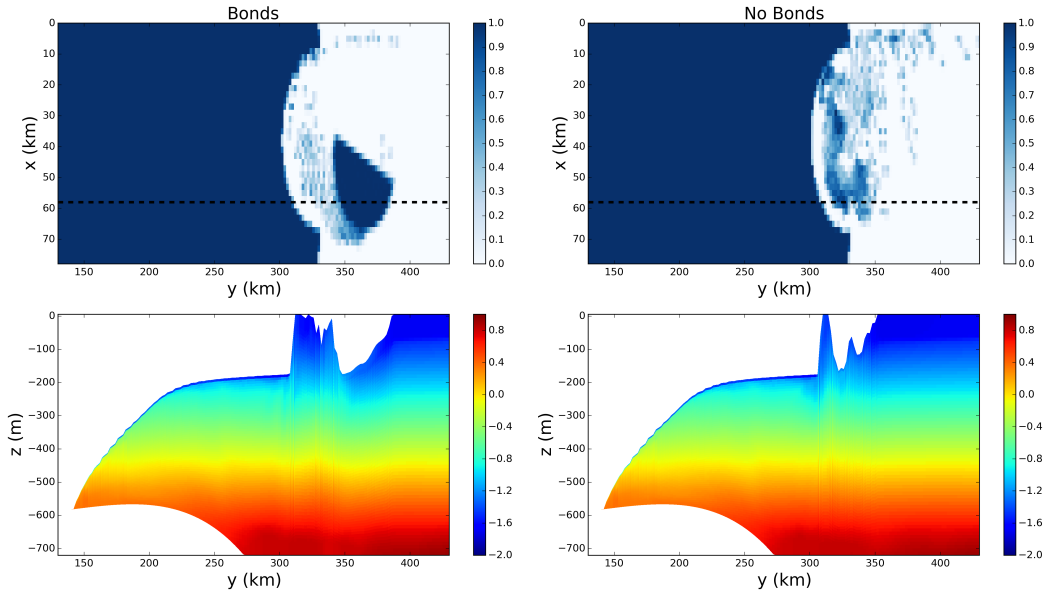
911 **Figure 7.** Snapshots of vertical sections of ocean temperature at  $x = 58$  km in the LBIM tabular iceberg  
912 calving experiment. Snapshots are taken (a) 7, (b) 15, and (c) 30 days after calving. The position of the  
913 vertical transects is shown by the dashed lines in Figure 2c.



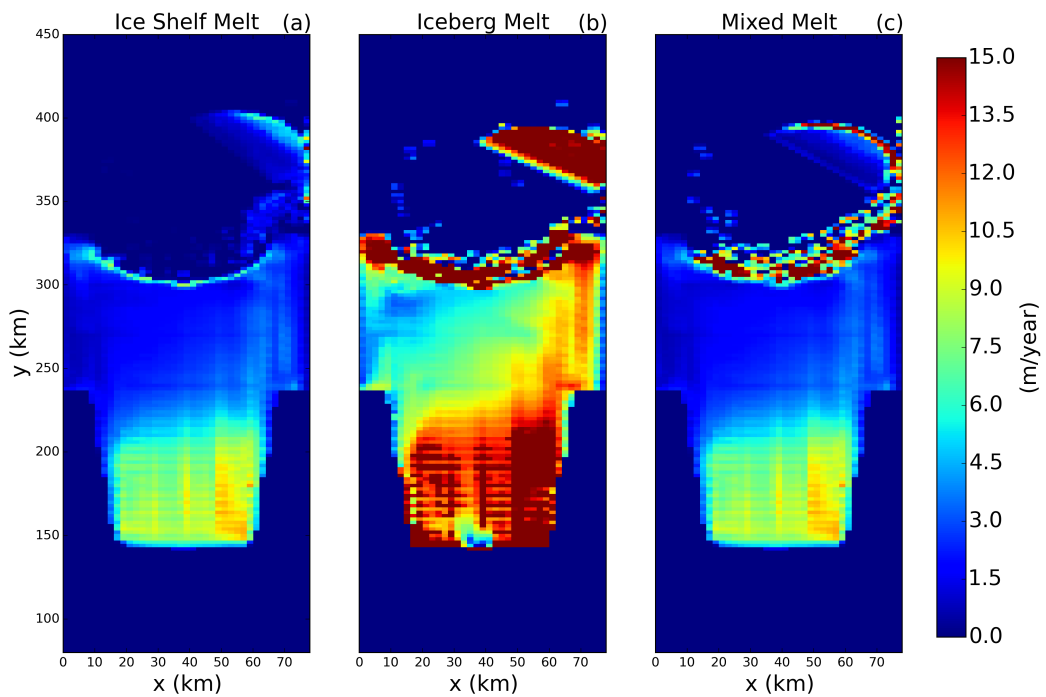
914 **Figure 8.** Snapshots of vertical sections of meridional velocity at  $x = 58$  km in the LBIM tabular ice-  
 915 berg calving simulation. Snapshots are taken (a) 7, (b) 15, and (c) 30 days after calving. The position of the  
 916 transects is shown by the dashed line in Figure 2c.



917 **Figure 9.** Results of the tabular iceberg calving simulation 30 days after the iceberg calves. The three panels  
918 show snapshots of the (a) melt rate, (b) top-of-ocean temperature and (c)  $u^*$  at the base of the ice shelf.  
919 Fields are only shown in regions where the ice area fraction is  $\geq 0.8$ .



920      **Figure 10.** Results from the tabular iceberg calving experiment with and without iceberg bonds. The top  
 921      row shows the fractional ice cover for the simulations (a) with and (b) without numerical bonds. The bottom  
 922      row shows the corresponding vertical temperature section at  $x = 58$  km for the simulation (c) with and (d)  
 923      without bonds. The location of the vertical transects in panels (c) and (d) are shown by the dashed lines in  
 924      panels (a) and (b), respectively. All snapshots are taken at time  $t = 30$  days. The simulations use wind stress  
 925       $\vec{\tau} = <0.0, 0.05>$ .



926 **Figure 11.** Melt rate 30 days after calving for simulations using (a) three equation  
927 model, (b) icebergs drift parametrization, (c) a mixture between the two (as described in Section 2.5.)

928      **9 Supplementary Material**

929      The experiment configuration used to initialize the calving tabular iceberg simulation  
930      (in this study) is the same as that of the Ocean0 setup in the MISOMIP, with the follow-  
931      ing three changes made:

- 932      1. The ‘calving criteria’ used in the MISOMIP study (which states that all points in  
933      the ice shelf with thickness less than 100m are set to zero thickness) has not been  
934      used.
- 935      2. The ice shelf has been thickened on the flanks of the domain, so that the latitude of  
936      the grounding line increases away from the center of the ice shelf.
- 937      3. The ice shelf is configured to be symmetric about its meridional center line ( $x =$   
938       $\frac{L_x}{2}$ ). This was achieved by using the average of the left and right flanks of the ice-  
939      shelf thickness.

940      These three changes were made in order to make the circulation beneath the ice shelf eas-  
941      ier to interpret.